JGR Solid Earth

RESEARCH ARTICLE
10.1029/2023JB028621

Exploring the Dynamic Interactions Between the Southern San Andreas Fault and a Normal Fault Under the Salton Sea

Luis Iván Bazán Flores[1], Christodoulos Kyriakopoulos[1], David D. Oglesby[2], Aron J. Meltzner[3,4], Thomas K. Rockwell[5], John M. Fletcher[6], and Daniel Brothers[7]

[1]Center for Earthquake Research and Information (CERI), The University of Memphis, Memphis, TN, USA, [2]University of California, Riverside (UCR), Riverside, CA, USA, [3]Earth Observatory of Singapore, Nanyang Technological University, Singapore, Singapore, [4]Asian School of the Environment, Nanyang Technological University, Singapore, Singapore, [5]San Diego State University (SDSU), San Diego, CA, USA, [6]Centro de Investigación Científica y de Educación Superior de Ensenada (CICESE), Ensenada, Mexico, [7]U.S. Geological Survey (USGS), Santa Cruz, CA, USA

Key Points:

- Normal fault displacement under the Salton Sea might indicate rupture along the Southern San Andreas Fault
- San Andreas North-to-South rupture scenarios are more likely to trigger normal fault slip than South-to-North cases
- Normal fault modeled displacements are comparable to observed normal fault vertical offsets

Supporting Information:

Supporting Information may be found in the online version of this article.

Correspondence to:

L. I. Bazán Flores and C. Kyriakopoulos, lbznflrs@memphis.edu; christos.k@memphis.edu

Citation:

Bazán Flores, L. I., Kyriakopoulos, C., Oglesby, D. D., Meltzner, A. J., Rockwell, T. K., Fletcher, J. M., & Brothers, D. (2024). Exploring the dynamic interactions between the Southern San Andreas Fault and a normal fault under the Salton Sea. *Journal of Geophysical Research: Solid Earth*, *129*, e2023JB028621. https://doi.org/10.1029/2023JB028621

Received 22 DEC 2023
Accepted 16 OCT 2024

Author Contributions:

Conceptualization: Luis Iván Bazán Flores, Christodoulos Kyriakopoulos
Data curation: Luis Iván Bazán Flores, Christodoulos Kyriakopoulos
Formal analysis: Luis Iván Bazán Flores, Christodoulos Kyriakopoulos
Funding acquisition: Christodoulos Kyriakopoulos
Investigation: Luis Iván Bazán Flores, Christodoulos Kyriakopoulos
Methodology: Luis Iván Bazán Flores, Christodoulos Kyriakopoulos
Resources: Luis Iván Bazán Flores, Christodoulos Kyriakopoulos
Software: Luis Iván Bazán Flores, Christodoulos Kyriakopoulos
Supervision: Luis Iván Bazán Flores, Christodoulos Kyriakopoulos
Validation: Luis Iván Bazán Flores, Christodoulos Kyriakopoulos

Abstract We investigate the dynamic interactions between the Southern San Andreas Fault (SSAF) and a proximal normal fault (NF) beneath the Salton Sea in southern California. The NF, positioned near the SSAF terminus at Bombay Beach, exhibits 11–15 displacement events across 14 stratigraphic sequences, with a range of 0.2–1.4 m of vertical offset since ∼2–3 ka. Notably, four of these events may align temporally with SSAF earthquakes, raising questions about the possible interplay between the two faults. Utilizing dynamic rupture models, we analyze the coseismic interactions between the SSAF and NF, addressing under what conditions the SSAF induces slip on the NF. Our findings reveal that a suite of SSAF ruptures, particularly those propagating from north to south, can trigger slip on the normal fault and replicate observed vertical offsets. If the SSAF extends beneath the Salton Sea, earthquakes originating south of the NF intersection are less likely to trigger normal fault slip, although we cannot exclude this possibility. Some SSAF ruptures do not trigger discernible slip on the NF, rendering such events undetectable in the stratigraphic record. Our research contributes toward discussions regarding the seismic hazard in southern California, shedding light on the interplay between the SSAF and NF.

Plain Language Summary The Southern San Andreas Fault (SSAF) has not produced a large earthquake in more than 290 years and is considered overdue for its next earthquake. The accepted terminus of the SSAF is located close to Bombay Beach, California, where a dense network of extensional features (normal faults) has been identified below the Salton Sea and adjacent to the SSAF. Seismic reflection profiles along these normal faults indicate seismic activity in the last 2–3 thousand years and possible interactions with the SSAF. At least four normal fault events may coincide temporally with major SSAF earthquakes, making the normal faults possible indicators of past SSAF ruptures. We use computer-based simulations to study the interactions between the SSAF and one representative normal fault under the Salton Sea. Our models reproduce normal-faulting displacements comparable to the observations, allowing us to infer rupture characteristics of the SSAF, such as nucleation location, propagation direction, rupture depth, and fault pre-stress direction.

1. Introduction

1.1. General Overview

The Southern San Andreas Fault (SSAF) has not produced a major earthquake in more than 290 years (Biasi & Scharer, 2019; Philibosian et al., 2011; Rockwell et al., 2022). Considering its average recurrence interval of ∼180 ± 40 years (Philibosian et al., 2011), the SSAF appears to be overdue for its next large rupture (Hill et al., 2023). The mapped southern terminus of the San Andreas Fault is near Bombay Beach, California (e.g., Field et al., 2014; Plesch et al., 2007). However, lineaments of seismicity (Hauksson et al., 2022) suggest that the SSAF projects into the Salton Sea and continues southward into the Brawley seismic zone (BSZ). South of Bombay Beach, the SSAF steps toward the Imperial fault (IF) to the southwest (Figure 1). The SSAF-IF step-over represents the transition from oblique divergence in the Gulf of California to transpression along the San Andreas Fault system (Crowell et al., 2013). The plate boundary deformation in the step-over has been attributed to dextral shear and block rotation (Crowell et al., 2013; Nicholson & Seeber, 1989; Nicholson et al., 1986) as suggested by thermal anomalies and late Quaternary volcanism under the southern Salton Sea (Elders et al., 1972; Fuis et al., 1984; Newmark et al., 1988), kinematics of ruptures in the area (Hudnut, Seeber, & Rockwell, 1989;

Visualization: Luis Iván Bazán Flores, Christodoulos Kyriakopoulos
Writing – original draft: Luis Iván Bazán Flores, Christodoulos Kyriakopoulos
Writing – review & editing: Luis Iván Bazán Flores, Christodoulos Kyriakopoulos, David D. Oglesby, Aron J. Meltzner, Thomas K. Rockwell, John M. Fletcher, Daniel Brothers

Hardebeck & Shearer, 2003) and seismicity patterns (Hauksson et al., 2017; Lin et al., 2007; Nicholson et al., 1986).

1.2. Deformation and Seismicity in the Brawley Seismic Zone

The continuous deformation in the BSZ is expressed through profuse microseismicity, seismic sequences, and swarms (Hauksson et al., 2017; Johnson & Hadley, 1976; Vidale & Shearer, 2006), often accompanied by aseismic phenomena (Chen & Shearer, 2011; Lohman & McGuire, 2007; Roland & McGuire, 2009). Rapid subsidence (Crowell et al., 2013), young volcanism (Schmitt & Vazquez, 2006), and geothermal production (Barbour et al., 2016) further contribute to the observed deformation and seismicity rates. A distinctive characteristic of the BSZ is an "array" of left-lateral cross faults organized on a ladder-type structure to the southeast of Bombay Beach (Hauksson et al., 2022; Sahakian et al., 2016). Depending on their adjacency to the SSAF and rupture depth, $M > 5$ earthquakes along the cross-faults might function as the initiation mechanism for a major SSAF earthquake in this area (Kyriakopoulos & Oglesby, 2024). Interestingly, seismic sequences in the BSZ do not align with the trend and sense of displacement along the mapped fault traces by Brothers et al. (2009), suggesting they result from perturbed stress fields connected to geothermal activity (Brodsky & Lajoie, 2013) and aseismic creep (Lohman & McGuire, 2007; Roland & McGuire, 2009). Although strike-slip motion is predominant, seismic sequences in the BSZ can also include normal fault events, such as the June 2000 swarm in the Mesquite Basin (Mw 4.1) and the August 2020 swarm in the southern Salton Sea (Mw 4.6) (Hauksson et al., 2022). Besides swarms and small-to-moderate earthquakes, large (M ~ 7.0) historical ruptures (Crowell et al., 2013; Hudnut, Seeber, & Rockwell, 1989) have occurred in the outskirts and periphery of the BSZ. Examples include the most recent ruptures of the Imperial fault, the Mw 6.9 1940 El Centro earthquake (Ulrich, 1941), and the Mw 6.5 1979 Imperial Valley earthquake, which was able to rupture two strands in the BSZ (Archuleta, 1984; Stover & Coffman, 1993). In addition to the Imperial fault earthquakes, the 1987 Ms 6.2 Elmore Desert Ranch and Mw 6.6 Superstition Hills earthquakes (Hudnut, Seeber, Rockwell, Goodmacher, et al., 1989; Magistrale et al., 1989; Sharp et al., 1989) occurred immediately west of the BSZ.

1.3. The Salton Sea

The Salton Sea was formed by an accidental, human-made diversion of Colorado River floodwaters in 1905 (e.g., Waters, 1983), although Ross (2020) presents evidence supporting a natural formation. It is located within the footprint of ancient Lake Cahuilla, the name used to define episodic past diversions (also referred to as Lakes) from the Colorado River into the Salton Trough (Philibosian et al., 2011; Waters, 1983). Most of these diversions may have filled the basin, reaching a +13 m highstand elevation. The lakes eventually desiccated, leaving distinctive sedimentary deposits, with the last inundation happening ~290 years ago (Philibosian et al., 2011; Rockwell et al., 2018, 2022). The substantial volume of sediments transported by these overflows has buried the fault surface expressions within the step-over region, inferred mainly from seismicity (Hauksson, 2000; Hauksson et al., 2022). Therefore, it is exceptionally challenging to provide constraints on the rupture history of the SSAF through the BSZ and consequently provide a more accurate estimation of the seismic hazard in this area.

1.4. Fault Connectivity

Due to the scarcity of direct mapping of fault surface expressions, the connectivity between major faults, such as the IF, SSAF, and San Jacinto (SJF) faults, still needs to be fully elucidated. Some studies suggest that the SJF fault system in the BSZ, which includes the Coyote Creek (CCF) and Superstition Hills (SHF) faults connect with the SSAF system (Janecke et al., 2011; Jennings & Bryant, 2010; Kirby et al., 2007) via the Extra fault (EF) that strikes ~N45°E (Figure 1). The EF intersects the CCF, which is located west of the Elmore Ranch fault (ERF), and strikes N50°W. Similarly, the ERF (strike ~N40°E), which intersects the SHF (strike N55°W), is thought to continue under the Salton Sea (e.g., Hudnut, Seeber, & Rockwell, 1989; Jennings & Bryant, 2010). This is probably the same structure that Brothers et al. (2022) refers to as the "Niland fault" (strike ~N10°E), which reaches the intersection with the southward projection of the SSAF. However, the regional kinematic significance of the ERF and EF, as well as their relation with offshore faults, are poorly understood (Brothers et al., 2009; Dorsett et al., 2019; Hudnut, Seeber, & Pacheco, 1989; Nicholson et al., 1986). For example, the azimuth of these faults may change when entering the SSAF-IF stepover to accommodate extension below the Salton Sea, or they might be completely separated structures (Brothers et al., 2022).

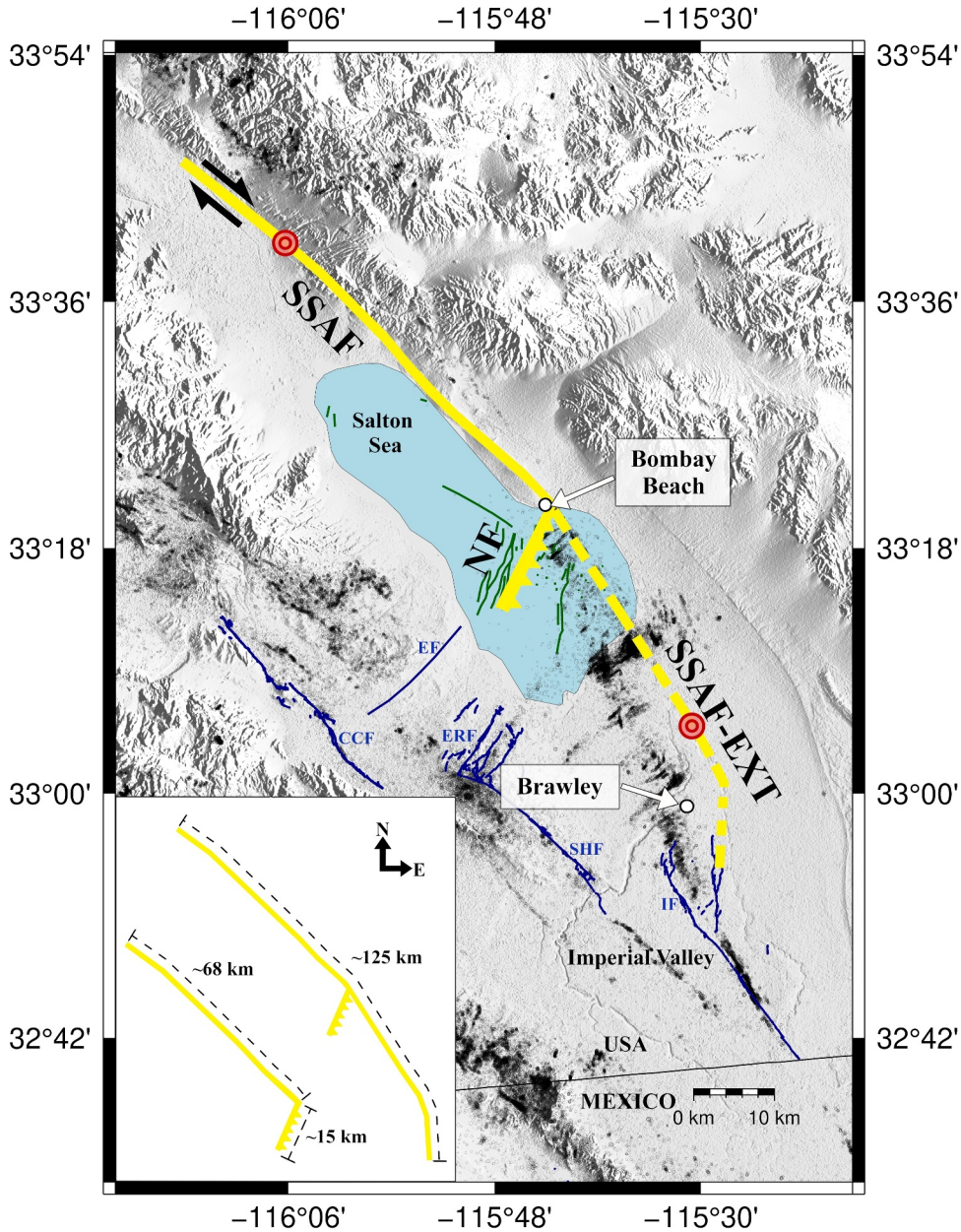

Figure 1. Map view of the Salton Sea and fault geometry used in our simulations. The continuous and dashed yellow lines highlight the faults implemented in our numerical models: Southern San Andreas Fault (SSAF), extended Southern San Andreas Fault (SSAF-EXT; overlapping with the SSAF north of Bombay Beach), and normal fault (NF). The SSAF and SSAF-EXT are vertical faults, while the NF dips at 65° toward the southeast. The white inset (bottom left corner) shows the two geometries used in our simulations. Mapped historical fault traces are shown with dark blue lines (U.S. Geological Survey and California Geological Survey, 2006), EF: Extra fault, CCF: Coyote Creek fault, ERF: Elmore Ranch fault, SHF: Superstition Hills fault, IF: Imperial fault. The green lines represent the network of normal faults under the Salton Sea (Brothers et al., 2009). The black-contoured circles represent seismic activity from 1981 to 2022 using the Southern California Earthquake Data Center (SCEDC) relocated catalog (Hauksson et al., 2012). The red concentrical circles mark the different nucleation locations used in our dynamic rupture simulations.

Finally, it is still not clear how or even if the SSAF and IF link in the BSZ. Dorsett et al. (2019) modeled plate deformation in the Imperial Valley and calculated long-term slip rates produced by models with different degrees of fault connectivity in the SSAF-IF system, favoring the direct linkage of the SSAF's southern terminus and the IF's northern terminus. Connection between major faults in the BSZ would facilitate joint rupture, increasing the

seismic hazard in the region. Indeed, Kyriakopoulos et al. (2019) showed that if connectivity between the SSAF and the IF exists in the BSZ, an earthquake starting on the IF can pass through the step-over toward the SSAF depending on the stress conditions of the faults and their dynamic interactions.

1.5. Normal Faults Under the Salton Sea

Brothers et al. (2009) used high-resolution seismic reflection profiles to identify a network of normal faults under the Salton Sea, striking ~N15°E and with an average dip of ~65° to the SE. Although the spatial extension of the normal faults is relatively well-imaged, gas obscures their mapping below a few dozen meters. The normal faults develop offshore immediately adjacent to the SSAF, west and south of Bombay Beach, and, as observed on high-resolution seismic reflection profiles, they offset Lake Cahuilla deposits from the last 2–3 ka (Brothers et al., 2011, 2022).

From this network, fault H7 is the most comprehensively mapped fault, and stands out for displaying the highest number of displacement events across 14 stratigraphic sequences (11–15), and a subtle seafloor scarp. The vertical offsets from these events range from ~0.2 to ~1.4 m (see Figures 11A and 13 of Brothers et al. (2022)). Notably, this fault is the closest to the terminus of the SSAF, extending over 10 km along the strike.

1.6. Possible Correlations Between SSAF and Normal Fault Ruptures

At least four of the normal fault events recorded by H7 are likely related to SSAF ruptures, with vertical offsets over 0.8 m, while another four potentially correlate to seismicity induced by flooding, showing offsets of less than ~0.4 m (Brothers et al., 2022). These correlations are based on the estimated dates for these events by Brothers et al. (2011, 2022), the timing of the last 5–7 Lake Cahuilla flood-desiccation cycles (e.g., Philibosian et al., 2011; Rockwell et al., 2022), and the most recent earthquakes along the SSAF (e.g., Brothers et al., 2011, 2022; Philibosian et al., 2011; Rockwell et al., 2018).

Correlating major SSAF ruptures and normal-fault displacements under the Salton Sea is an arduous task due to the few offshore and onshore sites from which direct samples and estimates of major SSAF ruptures are available. A better assessment of how normal faulting occurs in the Salton Sea requires an investigation of the dynamic coseismic interactions and the likelihood of a joint rupture with the SSAF. Joint ruptures of the two faults (e.g., considering faults H7 and SSAF) could occur either with initial nucleation on the SSAF and subsequent propagation on the normal fault or vice versa. In this study, we focus on the first scenario and address the second case (nucleation on the NF) in a subsequent manuscript (in preparation). If displacement on the normal faults indicates major SSAF ruptures, it becomes crucial to investigate the likelihood of such scenario and the main parameters controlling NF coseismic triggering. In the subsequent text, we use the term "triggering" to indicate "coseismic triggering," as delayed triggering is beyond the scope of this paper.

This work uses dynamic rupture models to understand the interaction between the SSAF and a representative normal fault (H7) in the BSZ. Fault H7 (Brothers et al., 2011), is the most comprehensively studied, and thus, the best candidate for implementation in our numerical experiments. Therefore, we focus our modeling efforts on predicting and discussing vertical offsets comparable to those observed along H7, and that occur during joint rupture with the SSAF.

The main questions addressed in this paper are the following: Are large SSAF events partly responsible for normal-fault displacement under the Salton Sea and which scenarios might be more likely? If yes, can we use the available observations to infer rupture properties, such as rupture direction?

To answer the above questions, we investigate what we consider to be among the main contributing factors to the coseismic activation of the NF. These include the length of the SSAF and its possible continuation South of Bombay Beach and under the Salton Sea. Additionally, because the locking depth is a determinant factor in generating a sustainable San Andreas rupture in the BSZ, we investigate the impact of a gradual decrease in the available fault rupture area. Furthermore, since we have no information regarding the directionality of SSAF ruptures in this area, scenarios with different hypocenter locations (north or south of Bombay Beach) are required to carefully evaluate the stress interactions between the two faults. Another topic of paramount importance is the direction and amount of slip generated during ruptures, which we address through appropriate considerations regarding the initial stress conditions and the regional kinematics in the BSZ.

2. Model Setup

2.1. Fault Geometric Configuration

Our models implement two faults: the SSAF and the normal fault (NF), which intersect close to Bombay Beach, the commonly accepted terminus of the SSAF (Field et al., 2014; Plesch et al., 2007). We also tested an alternative SSAF configuration that continues farther southeast, referred to as SSAF-EXT (extended SSAF). The SSAF and SSAF-EXT are based on the fault geometry of Kyriakopoulos et al. (2019), having lengths of 68 and 125 km, respectively (Figure 1). Both faults are vertical, compatible with the SCEC Community Fault Model v5.3 (preferred version), with an average strike of ∼N40°W (changing to N04°W near Brawley). The NF geometry is based on the proposed geometry for fault H7 in Brothers et al. (2011), with an along-strike length of 15 km, striking N25°E, and dipping 65° southeast. In this work, we often refer to the SSAF or SSAF-EXT simply as the "San Andreas Fault" and to their intersection with the NF simply as the "SSAF-NF intersection."

The typical finite element implementation of frictional contact requires that a grid node belongs only to a single slipping fault surface; thus, we must choose which fault is continuous through the intersection or branch point. In the case of the SSAF-NF intersection, we choose the SSAF-EXT to be a continuous through-going fault extending into the southern portion of the BSZ. Consequently, the slip on the SSAF-EXT is continuous and non-zero at the SSAF-NF "intersection" point, while the NF fault segment has a slip that tapers to zero. This approach might have a small effect on the slip near the intersection point, but it will not prevent the rupture from propagating onto the NF (DeDontney et al., 2012) and is unlikely to qualitatively change our results.

2.2. Mesh Configuration

The geometry and mesh of our 3D models (Figure 2; top panels) were generated using the advanced meshing software Trelis 17.0 (Coreform.com). The size of our finite element (FE) domain is ∼120 × 120 × 40 km and is composed of ∼17 million hexahedral elements. The mesh size is ∼150 m in the volumes enclosing the modeled faults and increases to ∼450 m or larger toward the outer boundaries of the model domain. We note that all ray paths between fault elements are entirely enclosed within the fine mesh region to allow accurate stress interactions at both short and long distances.

2.3. Locking Depth

In all our models, the locking depth is implemented by progressively increasing the effective normal stress below a fixed depth so that slip tapers to zero at the bottom of the fault (see Figure 2; bottom panels). Geophysical models discussing crustal thinning in the BSZ (Han et al., 2016; Persaud et al., 2016) and constraints provided by local seismicity (Hauksson et al., 2022) motivate us to investigate scenarios with both constant and variable locking depth. The selection of the locking depth determines the extent of the rupture fault area (seismic moment), which, in turn, will also determine the modeled NF vertical offsets resulting from each dynamic rupture scenario. Furthermore, we are motivated to investigate how a shallower locking depth might affect the ability of the SSAF to trigger NF slip.

2.3.1. Models With Constant Locking Depth

In all models presented in Sections 3.1–3.3, slip tapers to zero at a (locking) depth of between 14 and 15 km on the SSAF (or SSAF-EXT) (e.g., Nazareth & Hauksson, 2004; Smith-Konter et al., 2011) and 8 km on the NF (Figure 2e). The NF locking depth is based on the mean depth of seismicity under the Salton Sea and matches the source geometry used for the Coulomb stress calculation in Brothers et al. (2011). Note that a series of initial benchmark experiments where the NF has the same locking depth as the San Andreas are available in Figures S1 and S2 of the Supporting Information S1. While these initial experiments are not included in the main text due to space constraints, they are helpful in visualizing the impact of an shallower NF locking depth (15 vs. 8 km) on our simulations.

2.3.2. Models With Variable Locking Depth

Models in Section 3.4 use a variable locking depth (see Figure 2f). Hauksson et al. (2022) shows that in the southern portion of the Salton Sea (south of Bombay Beach), most seismicity occurs between ∼2 and ∼6 km depth. Moving southward, the seismicity depth increases again to 10 km as one approaches the Imperial fault.

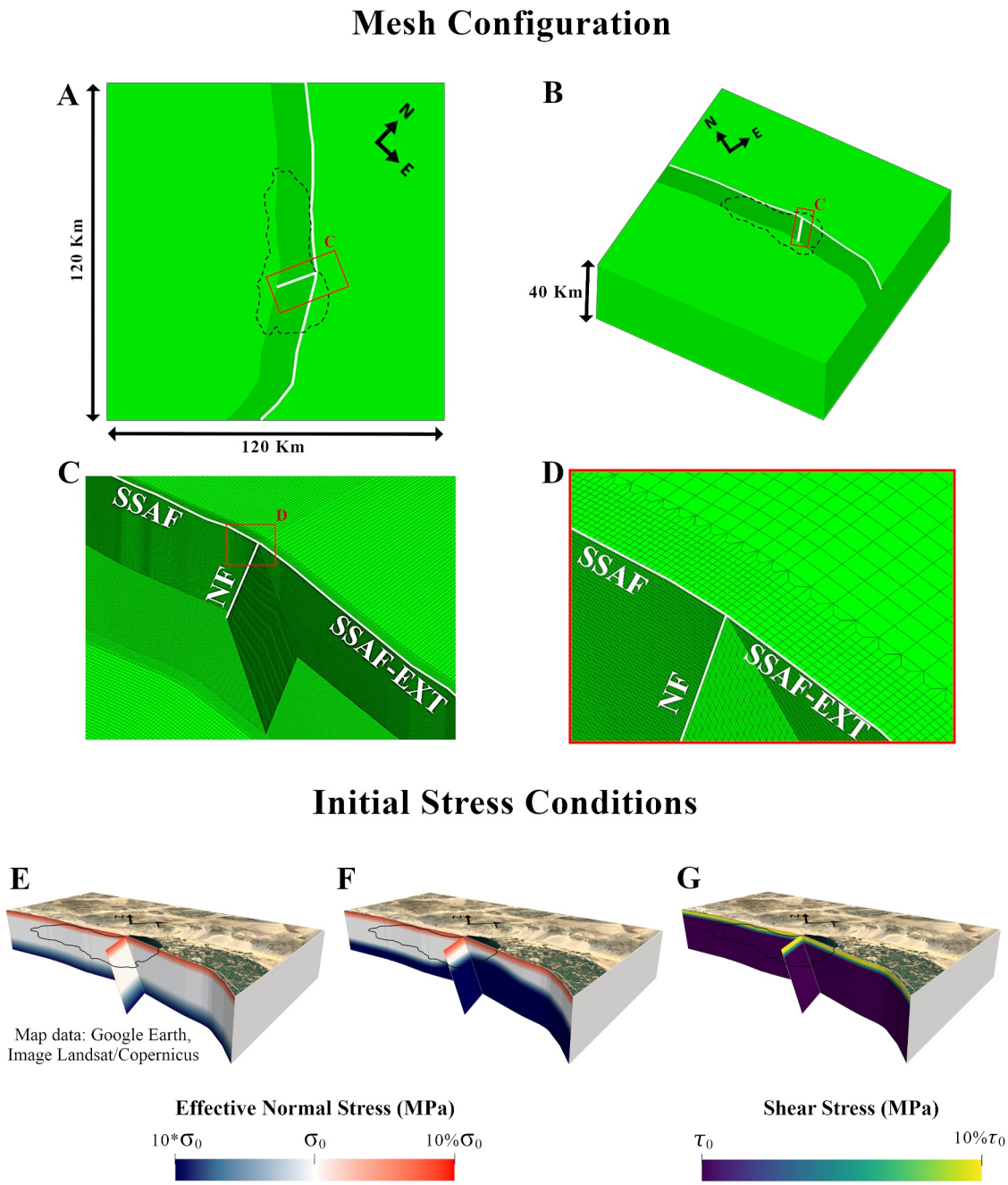

Figure 2. Finite element model and initial stress conditions. The Southern San Andreas Fault (SSAF and SSAF-EXT) geometries are based on Kyriakopoulos et al. (2019), while the normal fault (NF) is based on Brothers et al. (2011). Panels (a and b) show the full model domain in map and 3D view, respectively. Fault traces are indicated by white lines. The Salton Sea is indicated by the dotted black line and the continuous black lines in panels (e)–(g). Black arrows indicate north and east directions. Panel (c) shows a 3D view of the mesh. Panel (d) shows mesh details near the SSAF-NF intersection. Panels (e and f) show the initial effective normal stress (σ_0; hereinafter for brevity just "normal stress") for models with constant (~14–15 km) and variable locking depth (~3.5–~15 km) respectively. In both cases, the normal stress increases progressively toward the bottom of the fault. The effective normal stress is equal to the total normal stress on the fault plane minus the pore pressure. Panel (g) shows the initial shear stress (τ_0). The initial normal and shear stress values are reported in Table 1. Both initial normal and shear stresses are reduced near the free surface, from 3 to 0 km depth.

Using the above information, we generated a model (using the SSAF-EXT geometry) where the locking depth decreases from the north toward the SSAF-NF intersection (on both faults) at about 6 km depth. Toward the northern and southern limits of the SSAF-EXT, the locking depth increases to 15 and ~8 km, respectively. On the NF, the locking depth decreases from ~6 km near the SSAF-NF intersection to ~4 km at the opposite edge. This

model represents a smooth variation of the locking depth, which may be more appropriate than implementing it as an abrupt step.

2.4. Earthquake Nucleation

2.4.1. Hypocenter Location

We use two different nucleation locations along the San Andreas Fault to gain a first-order understanding of the effect of rupture directivity. The first hypocenter is placed at ∼45 km north of the SSAF-NF intersection, generating a north-to-south propagation (N2S). The second hypocenter is located at ∼32.5 km south of the intersection, producing a south-to-north propagation (S2N). Note that the second location is only possible for the SSAF-EXT configuration.

For the constant locking depth models, both N2S and S2N scenarios, the nucleation is fixed at 7.5 km depth. For the N2S variable locking depth cases, the nucleation depth remains 7.5 km, while the S2N cases require a shallower nucleation of ∼5 km on the southern portion of the SSAF-EXT.

2.4.2. Nucleation Procedure

In our dynamic rupture models, nucleation occurs artificially by increasing the shear stress to be 10% above the yield stress within an expanding nucleation radius. The size of this high-stress area, also called the critical patch, depends on the choices for the S parameter (and thus, the initial shear stresses), the stress drop, and the slip-weakening distance (see Equation 10 in Day (1982)).

We use a nucleation radius of 5 km for the experiments with constant locking depth, regardless of the nucleation location. For models with variable locking depth, we set the radius to be 5 km for the N2S cases and 3 km for the S2N cases due to the reduced along-dip width of the San Andreas.

2.5. Along-Strike Separation (Gap) Between the San Andreas and the NF

Normal faults under the Salton Sea might not extend far enough to the northeast to intersect the San Andreas Fault (see, Figure 2c of Brothers et al. (2022)) and have an along-strike length shorter than 15 km. Therefore, we test the effect of fault separation by implementing progressively increasing gaps of ∼0.5, 1, 2, 3, and 6 km between the San Andreas and the NF. These experiments use the SSAF-EXT configuration and variable locking depth. The motivation for these experiments is to gain a first-order understanding of the SSAF's ability to trigger NF slip over a separation gap for different nucleation locations and initial stress conditions. We should note for clarity that the introduction of a separation between the faults reduces correspondingly the along-strike length of the NF, and for example, a ∼3 km gap means that the NF is now ∼12 km in length instead of 15 km. To implement these gaps, we increase the normal stress on the corresponding NF segment (nodes) by a factor of one thousand, which effectively locks the nodes, inhibiting these patches from rupture. Results from these experiments are discussed in Section 3.4.

2.6. Initial Stress Configuration

A fundamental factor for classifying our simulations is the seismic parameter S (Andrews, 1976). S is the ratio of the strength excess over the expected stress drop (see Equation 1), where μ_s is the static coefficient of friction, σ_0 and τ_0 are the initial effective normal stress and shear stress, respectively, and μ_d refers to the dynamic coefficient of friction. For simplicity, in the following discussions, we refer to effective normal stress as "normal stress." We change S by modifying the magnitude of the initial shear stress (τ_0) while keeping the same normal stress (σ_0) in all the simulations presented in this paper. Therefore, lower S values indicate a fault closer to rupture (larger shear pre-stress), while higher S values indicate the opposite.

$$S = \frac{\mu_s * \sigma_0 - \tau_0}{\tau_0 - \mu_d * \sigma_0} \quad \frac{(\text{Strength Excess})}{(\text{Stress Drop})} \tag{1}$$

Finally, following Rice (1993), in all our models, we assume that from the free surface down to 3 km depth, the pore pressure increases hydrostatically, while below 3 km, the pore pressure increases at the lithostatic rate. Thus, starting at 3 km depth and toward the free surface, we linearly decrease the initial normal and shear stresses to 10%

Table 1
Physical and Numerical Parameters Used in Our Simulations

Simulation parameters		Values
Static coefficient of friction (μ_s)		0.6
Dynamic coefficient of friction (μ_d)		0.1
Slip weakening distance (m)		0.3
Density (kg/m^3)		2,700
S-wave speed (m/s)		3,162
P-wave speed (m/s)		5,477
Fault element Size (m)		~150
Off-fault element size (m)		~450
Number of time steps per second		100
Nucleation radius (m)		5,000*
* Note: Models with S2N propagation and variable locking depth use a smaller radius of 3 km		
Nucleation speed (m/s)		2,000
Initial shear stress in the nucleation zone (MPa)		6.44
Initial effective normal stress (σ_0; MPa) below 3 km		9.76
Initial shear traction (τ_0; MPa) below 3 km	SSAF or SSAF-EXT	NF
Sections 3.1–3.4	4.33 leading to $S = 0.45$	4.33 leading to $S = 0.45$
		2.6 leading to $S = 2.0$
	2.6 leading to $S = 2.0$	2.37 leading to $S = 2.5$
		2.19 leading to $S = 3.0$
Section 4	4.33 leading to $S = 0.45$	4.33 leading to $S = 0.45$
Calculated "a priori" stress drop (MPa) corresponding to the S values mentioned above	SSAF or SSAF-EXT	NF
Sections 3.1–3.4 and 4	3.35 ($S = 0.45$)	3.35 ($S = 0.45$)
		1.62 ($S = 2.0$)
	1.62 ($S = 2.0$)	1.39 ($S = 2.5$)
		1.22 ($S = 3.0$)

of their initial ambient value. Figure 2, bottom row, shows the map of initial stress conditions. The set of initial stresses and other numerical values used in our dynamic rupture simulations are reported in Table 1.

2.6.1. Direction of Initial Stress

In all our models, we set the initial shear stresses on the SSAF (or SSAF-EXT) consistent with a rake of 180°, representing right lateral motion, while for the NF we test cases beyond the pure normal motion. More specifically, in Sections 3.1 and 3.2, the NF has an initial shear stress direction consistent with a rake of −90° (pure normal motion) while Section 3.3 presents cases where the NF has an initial shear stress direction at −45° (oblique left-lateral motion) and 0° (pure left-lateral motion). Please note that in the oblique and left-lateral NF cases, the magnitude of pre-stress has been kept the same as in models with pure normal motion and only the orientation has been modified.

Models with oblique or left-lateral NF motion are motivated by the debate regarding the kinematics of the normal faults under the Salton Sea; the throw plots presented by Brothers et al. (2022) cannot discriminate between pure normal or oblique normal fault slip. Previous studies suggest that oblique motion can help to accommodate rapid subsidence (e.g., Lohman & McGuire, 2007; Roland & McGuire, 2009) in the BSZ due to extension in this young pull-apart basin (Brothers et al., 2009; Larsen & Reilinger, 1991). Additionally, the left-lateral strike-slip ERF,

and EF, which trend ~ N45°E, appear to reach the southwest shoreline of the Salton Sea with a similar strike direction and in proximity to our modeled NF.

Furthermore, resolving the regional stress tensor (e.g., Yang & Hauksson, 2013) into our fault geometry produces a right-lateral SSAF (rake of 180°) and an oblique NF (left-lateral and normal). The experiments with oblique NF pre-stress allow us to investigate how changes in the initial shear stress direction affect the magnitudes of the modeled vertical offsets. Section 3.4 presents a selection of experiments that include pure normal motion on the NF, as well as oblique and left-lateral cases. Section 4 assumes pure normal motion on the NF.

Finally, we should note that the dynamic rupture process generates rake rotation. Therefore, the slip may rotate significantly from the direction of the initial applied shear traction. Section 4 is dedicated to describing dynamic rake rotation phenomena.

2.6.2. Pre-Stress Amplitude: Sections 3.1–3.4

We defined the initial stresses for the San Andreas in such a way that our simulations produce displacements of a few meters inside the range of the expected strike-slip displacements for future SSAF events (e.g., Fialko, 2006; Weldon et al., 2002). From the initial stresses in the model, we can calculate S and the a priori stress-drop values that do not account for the time variability of normal and shear stress during rupture. The initial effective normal stress for the SSAF (or SSAF-EXT) and the NF is constant across all the simulations presented in this paper and equals 9.76 MPa.

The initial shear stress on the San Andreas (see Table 1) lead to two S values: $S = 0.45$ for a super-shear rupture (high shear pre-stress) and $S = 2.0$ for a sub-shear rupture (lower shear pre-stress). For the NF, we use two additional shear stress initial magnitudes leading to S values of 2.5 and 3.0 and correspond to a priori stress drops in the range of expected values in our study area (Chen & Shearer, 2011). Hence, in our experiments, the initial shear stress on the NF can differ from that on the San Andreas. Using these values, our suite of experiments produces vertical offsets comparable to the displacement events observed by Brothers et al. (2022). We refer the reader to Table 1, which shows the shear stress magnitudes for the S values mentioned earlier and their corresponding a priori stress drops for each group of experiments.

We note that the a priori calculated stress drop values are modified by the dynamic rupture process. The fault experiences time-dependent normal and shear stress changes induced mainly by variations in fault geometry (e.g., changes in strike direction), free surface effects (e.g., amplification of fault slip rate), dynamic overshoot, and fault-to-fault interaction. Therefore, constant traction models will eventually produce a spatially heterogeneous stress drop, different from the a priori calculated values, and consequently, a heterogenous slip distribution.

Finally, we also note that additional N2S experiments where our fault system is pre-stressed using regional stress information are available in Supporting Information S1. These models assume relatively low, medium, and high initial stress magnitudes, imposing heterogeneous initial stress conditions along the strike on both faults. In these experiments, the initial stress field is consistent with the SHmax orientation (~10° East of North) in the BSZ (Yang & Hauksson, 2013).

2.6.3. Pre-Stress Amplitude: Section 4

Section 4 investigates the process of dynamic rake rotation imparted on the NF by rupture on the San Andreas. In this section, both faults are highly prestressed ($S = 0.45$).

2.7. Coulomb Failure Stresses (ΔCFS)

Ruptures traveling N2S and S2N along the San Andreas Fault display significant differences regarding their dynamic interaction with the NF. To study these differences, we calculate Coulomb failure stress changes (ΔCFS; Equation 2; Harris & Simpson, 1992; King et al., 1994; Lin & Stein, 2004) at each simulation time step and carefully evaluate the effect of SSAF ruptures over the NF.

$$\Delta \mathrm{CFS} = \Delta \tau_{\mathrm{shear}} + \mu_s * \Delta \sigma_{\mathrm{normal}} \tag{2}$$

where $\Delta\tau_{shear}$ and $\Delta\sigma_{normal}$ represent on-fault changes in shear stress and effective normal stress, respectively, and μ_s is the static coefficient of friction. In Sections 3.2 and 3.4, we plot time snapshots of fault slip on the two faults jointly with ΔCFS values on the NF caused by slip in the SSAF.

2.8. Frictional and Material Properties

The friction law used to model the rupture process is linear slip weakening (Andrews, 1976; Ida, 1972), where the friction coefficient drops from a static value (μ_s) of 0.6 to a dynamic value (μ_d) of 0.1 (Di Toro et al., 2011) over a slip weakening distance of 0.3 m. The numerical values used in our numerical simulations are reported in Table 1. The outcome of each simulation is composed of the time series of several rupture parameters, such as fault slip, fault slip rate, and normal and shear stress changes. We assume a homogenous and isotropic half-space with Vp of 5,477 m/s, Vs of 3,162 m/s, and density of 2,700 kg/m^3.

2.9. Dynamic Rupture Code

To run our rupture experiments, we use the publicly available dynamic rupture code FaultMod (Barall, 2009; https://code.usgs.gov/esc/faultmod). The code has been repeatedly validated against other dynamic rupture codes within a multiyear collaborative exercise, the SCEC/USGS Dynamic Rupture Technical Activity Group (Harris et al., 2009, 2018). FaultMod solves the full elastodynamic problem, which includes inertial waves, and the static stress transfer as the long-time-limit after all waves have disappeared from the model domain.

3. Dynamic Rupture Results

In this section, we describe whether and under what conditions SSAF ruptures can trigger slip on the NF. Toward this goal, in Sections 3.1–3.3, we run a series of initial models that allow us to infer first-order interactions between the two faults. Our subsequent investigation builds on top of the initial experiments to progressively explore more complex (e.g., using variable locking depth) models in Section 3.4.

The large number of simulations (over 150) run for this study prohibits us from presenting and discussing extensive details of each model. For that reason, we discuss simulations that we believe best represent the main findings from each group of experiments. Specifically, for each selected model, we present the final slip (after 90 s of simulation) and corresponding modeled NF vertical offsets that we compare with the available observations. The final seismic moment of our models (e.g., ∼Mw 7.3 for our high stress constant locking depth cases) is limited by the dimensions of the SSAF and SSAF-EXT in the finite element mesh and should be considered a lower bound for earthquakes that could extend beyond the fixed boundaries of our model space.

To facilitate the comparison between observations and model predictions, all our figures showing final slip include a scale with the modeled vertical displacement of each experiment, extracted at the mid-point of the NF slip patch at the free surface (depth = 0), and the range of values reported by Brothers et al. (2022). Table S2 in Supporting Information S1 summarizes all the numerical results discussed in the main text and Supporting Information S1.

3.1. Nucleation on the SSAF With North-To-South Rupture Propagation (N2S)

We nucleate earthquakes on the SSAF north of the intersection with the NF, and we allow rupture to extend down to a depth of ∼14–15 km on the SSAF and 8 km on the NF, producing an N2S rupture propagation. The initial shear stress direction for the SSAF corresponds to a purely right lateral fault (rake 180°) while the NF is pre-stressed to pure normal motion (rake = −90°).

All our models with $S = 0.45$ on the SSAF (Figures 3a and 3b) or SSAF-EXT (Figures 3f and 3g) trigger slip on the NF and the rupture propagates throughout the entire NF area regardless of the S value on the NF. The magnitude of triggered slip on the NF, and consequently the vertical offset at the free surface, decreases with higher S values on the NF (visible by scanning Figure 3 from top to bottom). For example, models with $S = 0.45$ on the NF produce vertical displacement (subsidence) at the free surface of ∼1.7 m (SSAF; Figure 3a) to ∼1.5 m (SSAF-EXT; Figure 3f) and decrease to ∼0.97 m (Figure 3b) and ∼0.64 m (Figure 3g) when the NF prestress is such that $S = 3.0$. These values represent reductions of ∼43% and ∼56%, respectively and highlight how the initial shear stress plays a critical role on the amount of predicted NF vertical displacement.

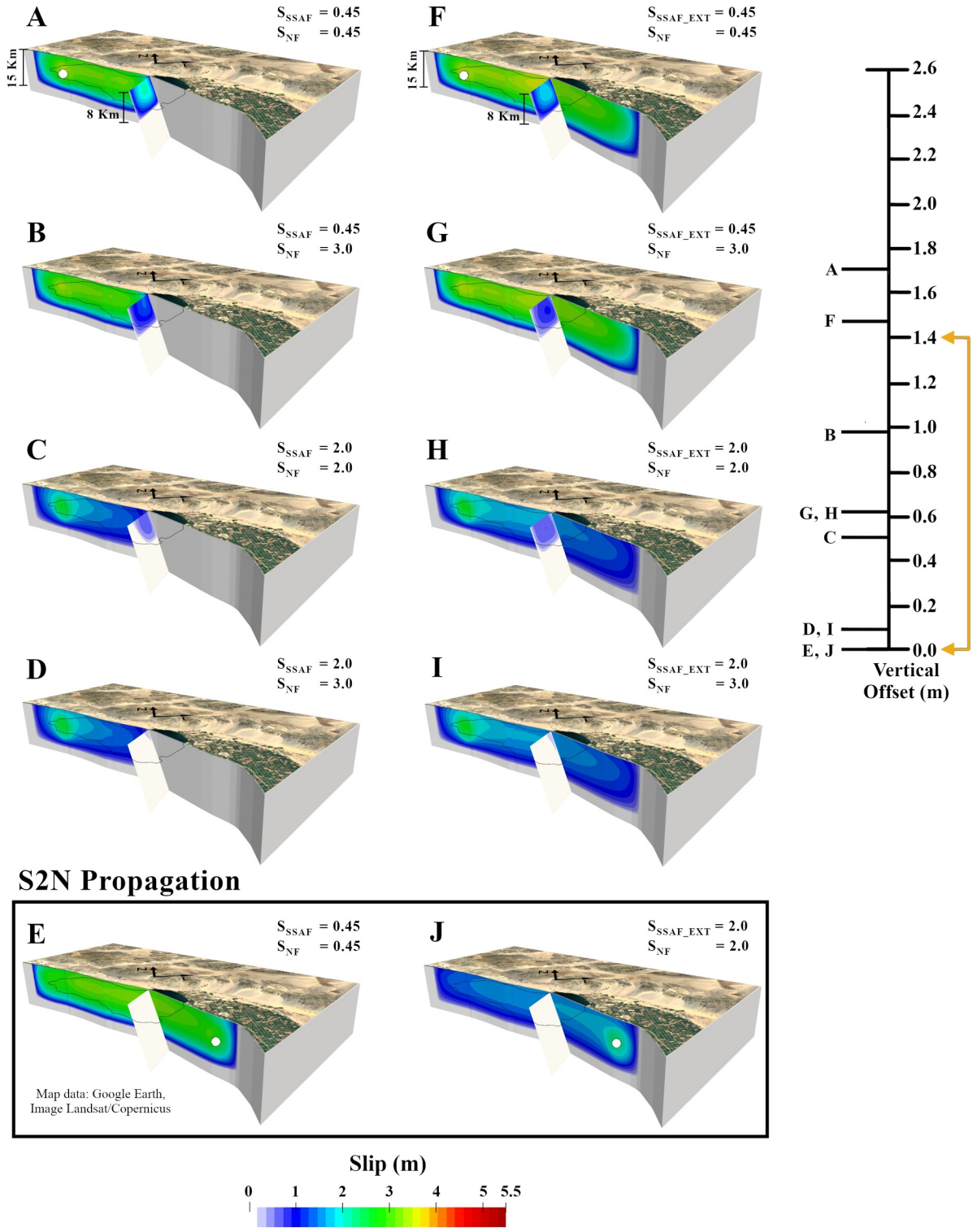

Figure 3.

We also test cases in which the SSAF (Figures 3c and 3d) or SSAF-EXT (Figures 3h and 3i) are prestressed at a lower shear stress level such that $S = 2.0$. Contrary to the previous cases, only one model shows a rupture of the entire NF area (Figure 3h), while the model in Figure 3c produces a partial NF rupture. Reducing the NF shear pre-stress, such that $S = 3.0$, results in negligible slip, barely visible on the NF (Figures 3d and 3i) near the SSAF-NF intersection.

Across all the experiments ran using constant locking depth and a highly prestressed San Andreas, experiments show a range of vertical offsets between ∼0.11 and ∼1.7 m. On the other hand, experiments with lower SSAF shear pre-stress show maximum vertical displacements of ∼0.62 m, but generally display reduced or completely absent NF slip. Figure S3 in Supporting Information S1 shows additional intermediate cases ($S = 2.0$ and 2.5 on the NF) for the rupture scenarios presented in this section.

3.2. Nucleation on the SSAF With South-To-North Rupture Propagation (S2N)

Here, we present experiments with nucleation locations south of the SSAF-NF intersection, only possible if the San Andreas extends further south under the Salton Sea (SSAF-EXT configuration). The fault geometry and locking depth are the same as in Section 3.1.

Simulations from this section are presented in the bottom part of Figure 3 (panels 3e and 3j). Interestingly, when the rupture propagates from south to north, the San Andreas does not trigger slip on the NF under any initial shear stress conditions. Further simulations with NF prestressed at a lower shear stress level (e.g., leading to $S = 2.5$ and 3.0) were not necessary since they would not change the outcome of our S2N simulations.

A simple explanation of why N2S and S2N cases produce opposite results can be inferred by examining the time-dependent stress radiated from the SSAF-EXT to the NF presented in Figure 4. A rupture traveling on the San Andreas and approaching the NF from the north (Figures 4a and 4b) increases the shear stress in the direction of the NF prestress, while at the same time decreasing the normal stress (NF unclamping). The shear and normal stress changes combine into a positive ΔCFS, increasing the likelihood of NF slip as the rupture approaches from the north. This effect is flipped when the rupture front passes the intersection with the NF (Figures 4c and 4d) and continues southwards toward the end of the fault model. After this time, normal stress increases (clamping), and shear stress decreases on the NF, creating unfavorable conditions that eventually combine into a negative ΔCFS. Thus, the amount of rupture travel time ahead of and beyond the intersection as well as the distribution and magnitude of slip, play significant roles in the triggering (or lack thereof) of the NF. In most of our N2S simulations, rupture passes from the SSAF to the NF before it crosses the SSAF-NF intersection. Thus, the switch from favorable to unfavorable conditions on the NF is not fast or strong enough to interrupt the ongoing rupture on the NF. However, the final amount of slip observed on the NF does depend on the stress changes imparted by the rupture propagating south of the intersection. A rupture propagating southward of the SSAF-NF intersection will disrupt the development of NF slip, as seen by the lower slip in the SSAF models in Figures 3f and 3g compared to the SSAF-EXT models in Figures 3a and 3b.

Similar stress interactions take place in the S2N scenario (Figures 4e–4h), although the order of events is reversed as rupture initiates south of the SSAF-NF intersection. Rupture on the SSAF-EXT approaching the NF from the south increases the normal stress and decreases the shear stress in the direction of the NF's prestress, generating unfavorable conditions (negative ΔCFS) for slip on the NF, except for small zones of limited amplitude near the fault intersection (Figures 4e and 4f). When the rupture front crosses to the north of the intersection with the NF,

Figure 3. Dynamic rupture simulations for models with a constant locking depth of ∼14–15 on the Southern San Andreas Fault (SSAF and SSAF-EXT), and 8 km on the normal fault (NF). The locking depth on each fault is marked with vertical bars. In panels (a)–(d), the San Andreas (SSAF) ends at the intersection with the NF (SSAF-NF intersection), while in panels (e)–(j) the San Andreas (SSAF-EXT) "extends" south of the SSAF-NF intersection. The black continuous line highlights the Salton Sea shoreline, while black arrows indicate North and East (N, E) directions. The four top rows show north-to-south (N2S) propagating ruptures, while the bottom row shows the south-to-north (S2N) scenarios. The nucleation location is marked at the top (panels a and f) and bottom (panels e and j) two panels with a white circle. The initial pre-stress conditions on each fault (see Table 1) lead to the S values indicated at the top right corner of each panel. The S value represents the ratio of the strength excess over the a priori stress drop (see Equation 1 in the main text); lower S values indicate a fault closer to rupture while higher S values indicate the opposite. The figure includes a scale (right side of figure) with the range of modeled vertical offsets for each panel, extracted at the mid-point of the NF slip patch at the free surface, as well as the range of values reported by Brothers et al. (2022) (double dark yellow arrows). Note that the NF final slip decreases with increasing S values (lower initial shear stress).

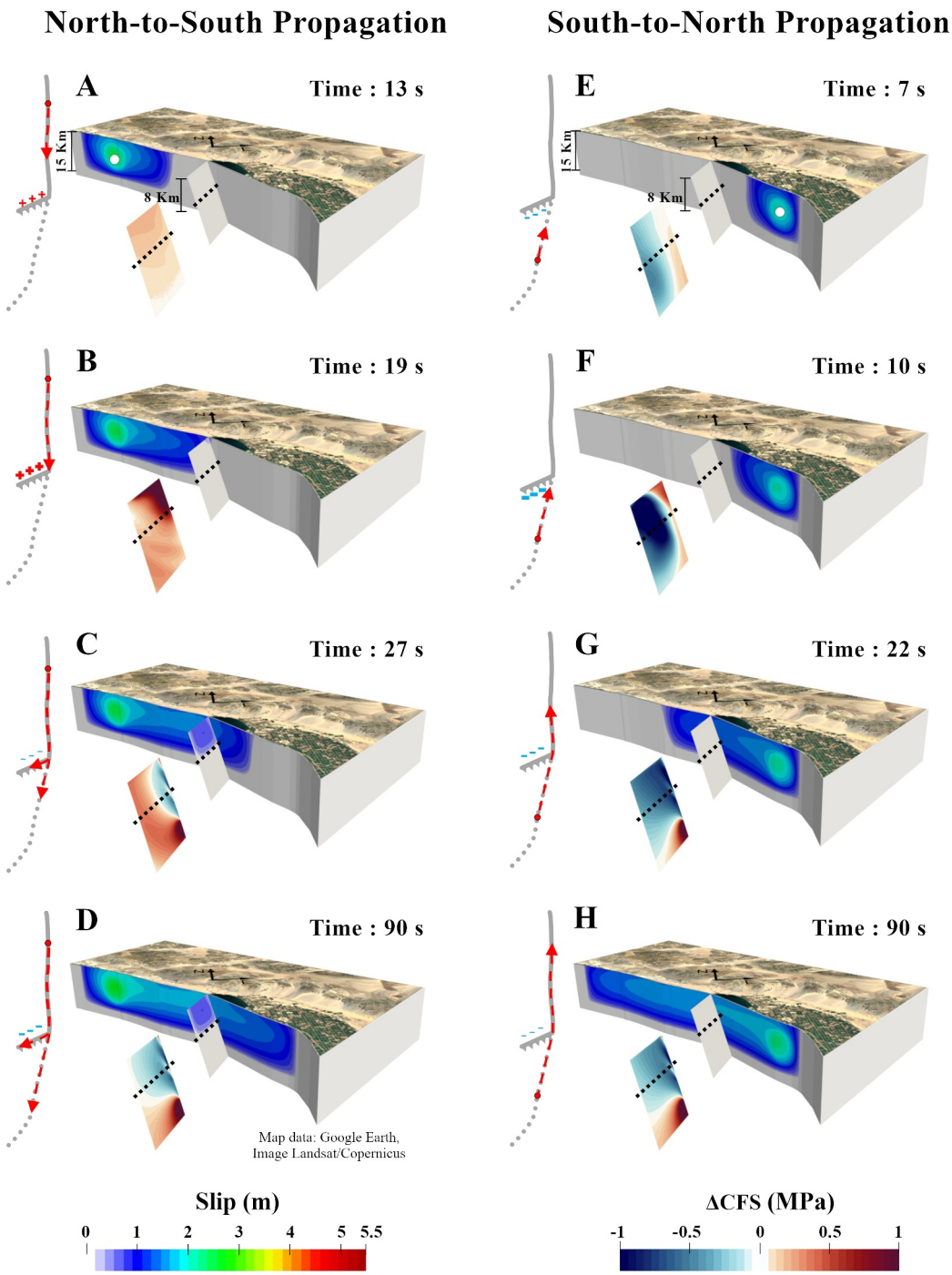

Figure 4. Time snapshots of Coulomb Failure Stress changes ($\Delta CFS = \Delta\tau_{shear} + \mu_s * \Delta\sigma_{normal}$) on the normal fault for ruptures traveling north-to-south (N2S) and south-to-north (S2N) on the San Andreas (SSAF-EXT model; for $S = 2.0$). Panels (a–d), left column, show the N2S case while panels (e–h), right column, show the S2N experiment. To highlight the relative position of the rupture front with respect to the SSAF-NF intersection (Bombay Beach) we show time snapshots of fault slip on the San Andreas. The imparted stress changes are mapped on the NF with a blue (negative ΔCFS) to red (positive ΔCFS) colormap. To facilitate the visualization of fault interaction, each panel includes a separate "detached" view of the ΔCFS changes on the NF. We observe positive ΔCFS values associated with the N2S propagation (panels a and b) until rupture reaches the intersection and starts propagating on the NF (panels c and d). On the contrary, the S2N case highlights the initial mostly negative ΔCFS (panels e–h), and rupture doesn't jump on the NF. In the N2S case, to avoid visualizing the effect of the stress drop accompanying the NF rupture that will obscure the change in ΔCFS, we plot ΔCFS changes as if the NF were not to rupture. Each panel includes a schematic representation (left side) of the NF ΔCFS change. The black dotted line shows the approximate bottom depth of the NF available rupture area. All symbols are the same as in Figure 3.

the effect is inverted and the ΔCFS increases progressively but without, however, reaching positive ΔCFS values (Figures 4g and 4h). Thus, we don't observe triggering of the NF in the S2N constant locking depth models.

We note that the choice of nucleation location along-strike is somewhat arbitrary. To provide an indication of the sensitivity of our results to the artificial nucleation location, we tested four additional models, N2S and S2N ruptures for $S = 0.45$ and $S = 2.0$ (shown in Figure S4 of the Supporting Information S1), with nucleation location closer to the intersection, about half the original along-strike distance. Moving the nucleation location does not change the ability of rupture to propagate to the NF. Thus, even if our models cannot capture the entire spectrum of possible nucleation scenarios, they provide a good qualitative understanding of the first-order behavior of the system.

3.3. Effects of Pre-Stress Rake Angle on the Normal Fault

Here we test cases in which the normal fault is prestressed to have oblique motion (normal + left-lateral; rake of −45°), and cases where the NF fault is prestressed to be purely left-lateral (rake 0°). The magnitude of pre-stress has been kept the same as in previous experiments; only the initial orientation has been modified in these models.

Compared to cases with $S = 0.45$ on both faults shown in Section 3.1, models with obliquely (normal + left-lateral) pre-stressed NF show decreased slip values. The combination of reduced slip magnitude and oblique motion translates to smaller vertical offsets. For example, the SSAF and SSAF-EXT models (Figures 5a and 5c) drop to values of ∼1.29 and ∼1.0 m, respectively, compared to the ∼1.7 and ∼1.5 m of their counterpart with normal (rake −90°) pre-stress (Figures 3a and 3f). These represent reductions of 24% and ∼33%, respectively. Note that for the same magnitude of slip, a fault with pure normal motion will generate stronger subsidence than the same fault with oblique motion. When we further reduce the pre-stress level such that $S = 2.0$ (Figures 5b and 5d) the San Andreas doesn't trigger slip on the NF.

When the NF is pre-stressed to be purely left-lateral (rake 0°; Figures 5e–5h), none of our N2S simulations show slip extending on the entire normal fault, and in only one case, we observe a limited slip patch near the SSAF-NF intersection (Figure 5e).

3.4. Simulations With Variable Locking Depth

Results from experiments with variable locking depth (Figure 6) show that for the high stress ($S = 0.45$) N2S models, the locking depth reduction doesn't preclude triggering of NF slip. Furthermore, we observe changes in the magnitude and spatial extension of slip on both faults, caused by the progressive reduction in the available rupture area (or equivalently seismic moment) near the SSAF-NF intersection. A smaller rupture area on the SSAF-EXT produces less slip impacting the stress transferred by the San Andreas to the NF. A smaller rupture area on the NF also imparts a reduction of its final slip. For example, in the $S = 0.45$ case (Figure 6a), we observe ∼1.17 m of modeled vertical offset, significantly lower than ∼1.7 m in the model presented in Figure 3a. A further reduction of vertical offset to 0.52 m is observed for a lower NF shear pre-stress value leading to $S = 3.0$ (Figure 6b).

As mentioned in Section 2.5, the normal faults under the Salton Sea might not reach or intersect the SSAF. Thus, we explore the effect of fault separation by implementing progressively larger gaps between the SSAF-EXT and the NF. Figure 6c shows a representative case with a ∼6 km separation while a larger collection of gap models is presented in Figure S5 of the Supporting Information S1. We find that for the high-stress models (leading to $S = 0.45$ on both faults), the separation between the two faults doesn't preclude rupture from jumping on the NF. Furthermore, the ability of rupture to propagate across gaps persists even for lower NF shear pre-stress, such that $S = 3.0$, and keeping the same ∼6 km separation (Figure 6d). The separation between the faults reduces the along strike NF length; for a 3 km gap the NF length decreases to 12 km instead of 15 km. Assuming the same initial shear stress, reductions in fault area correspond to reductions in final fault slip. Indeed, for the $S = 0.45$ models, the modeled vertical offsets decrease progressively with gap increases from 1.17 m (no gap; Figure 6a) to ∼0.7 m (6 km gap; Figure 6c) and drops below 0.2 m if combined with lower NF pre-stress such that $S = 3.0$ (Figure 6d).

Simulations with variable locking depth and oblique (−45°) or purely left-lateral (0°) NF pre-stress are consistent with findings and conclusions from Section 3.3. For that reason, we limit the number of results presented in the main text to four panels, Figures 6e–6g and 6o. Figure S6 in Supporting Information S1 provides additional models highlighting the effect of rotating the NF rake (from −90° to 0° in steps of 10°). Figure S7 in Supporting

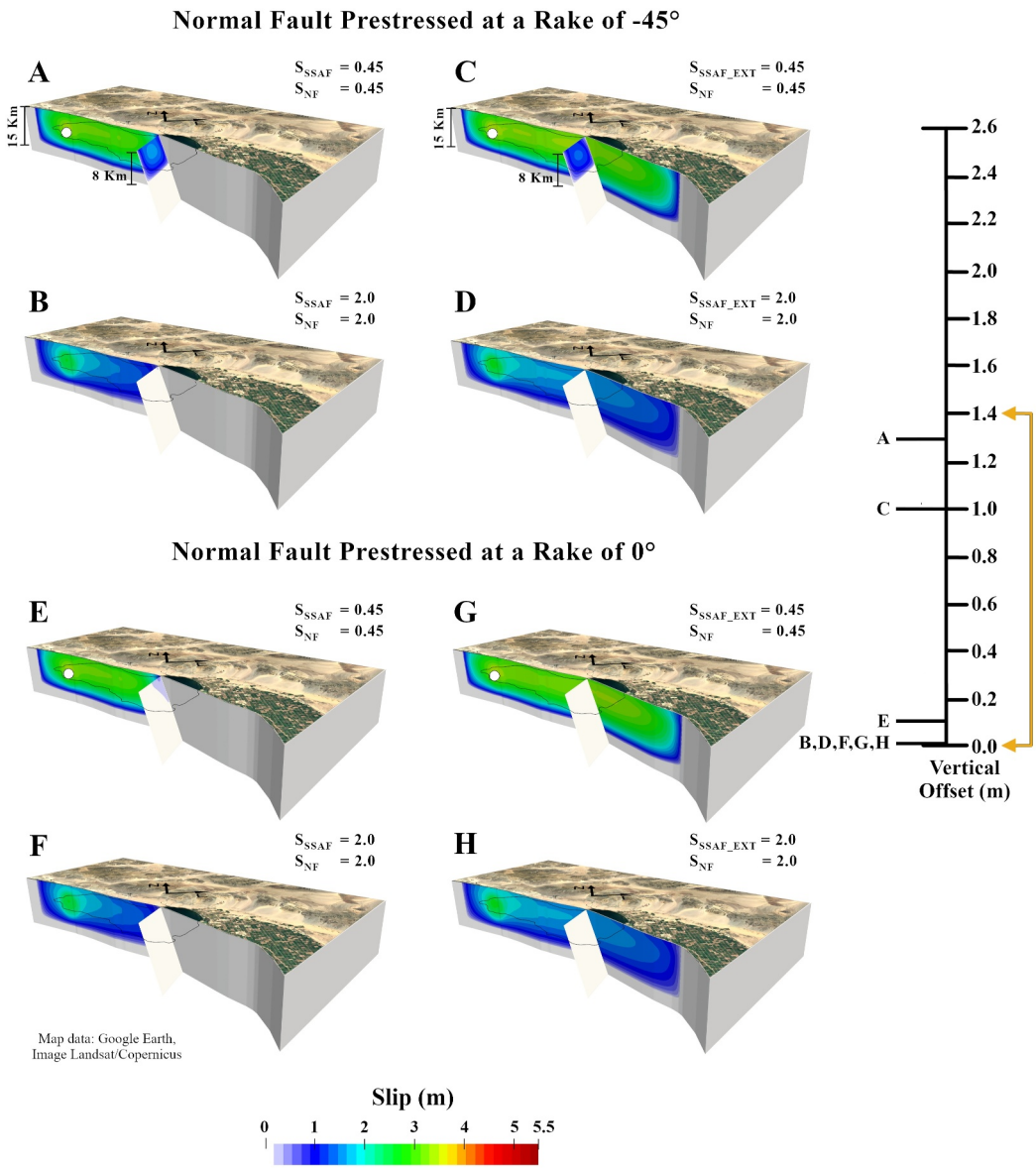

Figure 5. North-to-south (N2S) rupture simulations with oblique (−45°; panels a–d) and left-lateral (0°; panels e–h) normal fault (NF) pre-stress. In the left column (panels a, b, e, and f), the San Andreas (SSAF) ends at the intersection with the NF, while in the right column (panels c, d, g, and h), the San Andreas (SSAF-EXT) "extends" south of the SSAF-NF intersection. The first and third rows represent experiments with $S = 0.45$ on both faults, while for the second and bottom rows $S = 2.0$. The rotation of the initial direction of NF shear stress to include a left-lateral component disrupts the ability of the San Andreas to trigger slip on the normal fault relative to the pure normal faulting cases (e.g., Figure 3).

Information S1 shows additional models with oblique pre-stress and models combining oblique pre-stress with separation (gap) between the two faults.

Figure 6e ($S = 0.45$ on both faults) shows a model with NF initial shear stress direction at a rake of −45°. We observe ∼0.7 m of vertical NF displacement significantly reduced if compared to Figure 6a (1.17 m) in which the NF is pre-stressed to pure normal motion. Finally, Figure 6f shows an oblique model with a ∼6 km gap between the two faults in which rupture still propagates on the NF, and the modeled vertical offset is ∼0.2 m.

When we pre-stress the SSAF and NF such that $S = 2.0$ (Figure 6h) the modeled vertical offset is 0.35 m and drops further to ∼0.07 m for $S = 2.5$ on the NF (Figure 6i). Interestingly, for $S = 2.0$, the progressive reduction of fault available rupture area hinders rupture propagation south of the SSAF-NF intersection, and slip stops just a few

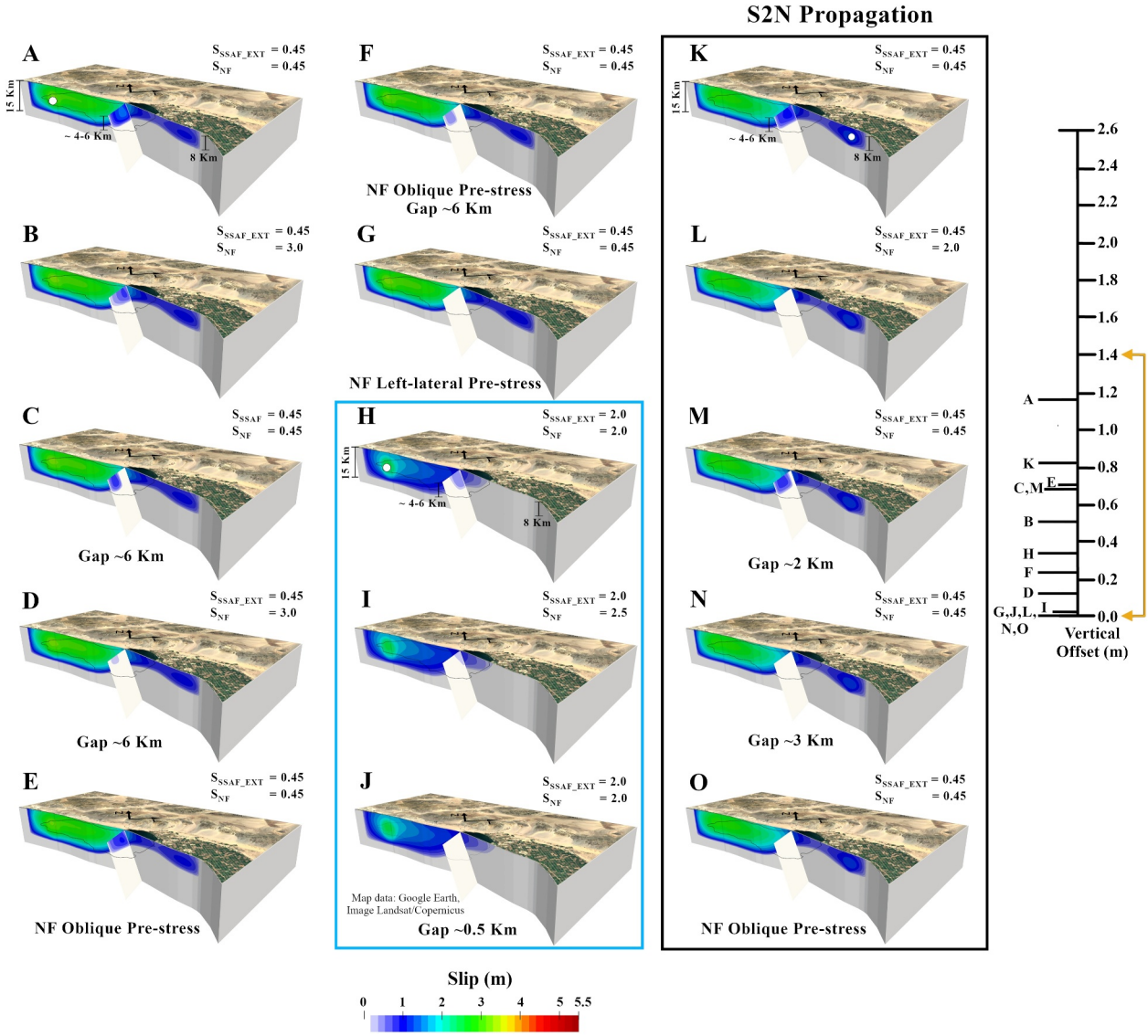

Figure 6. Dynamic rupture simulations for models with a variable locking depth. The locking depth limits are marked with vertical bars (panels a, h, and k). Panels (a–j) show north-to-south (N2S) experiments, while panels (k–o) show south-to-north (N2S) cases. The initial pre-stress conditions on each fault (see Table 1 for corresponding values) lead to the S values indicated at the top right corner of each panel. Panel (a) shows a model with $S = 0.45$ on both faults. In panel (b), we decrease the initial NF shear stress such that $S = 3.0$. Panel (c) implements a separation (gap) of ∼6 km between the two faults, keeping the same initial stress conditions of panel (a). Panel (d) implements the same stress conditions as panel (b) and includes a ∼6 km gap between the two faults. Panel (e) shows a model with $S = 0.45$ on both faults and oblique pre-stress (rake of −45°) on the NF. Panel (f) combines oblique NF pre-stress and a ∼6 km gap ($S = 0.45$ on both faults). Panel (g) shows a model with $S = 0.45$ on both faults and left-lateral pre-stress (rake of 0°) on the NF. The blue rectangle separates the N2S lower-stress experiments in panels (h)–(j). Panel (h) shows a model with $S = 2.0$ on both faults. In panel (i) we reduce the NF initial shear stress such that $S = 2.5$. In panel (j), $S = 2.0$ on both faults, a gap of ∼0.5 km inhibits NF rupture. The black rectangle separates S2N experiments in panels (k)–(o). Panel (k) shows a model with $S = 0.45$ on both faults. Contrary to what has been observed earlier for S2N ruptures (e.g., Figure 3e), we observe NF triggering. In panel (l), a lower initial NF shear stress (such that $S = 2.0$) prevents rupture from propagating onto the NF. Panels (m) and (n) show models with a ∼2 and 3 km gap respectively. Rupture propagates on the NF only in the first case. Panel (o) shows a model with $S = 0.45$ on both faults and oblique pre-stress (rake of −45°) on the NF. The oblique pre-stress inhibits the triggering of the NF. All symbols are the same as in Figure 3.

kilometers to the south (e.g., Figure 6i). On the contrary, in all our N2S $S = 0.45$ models (Figures 6a–6g), slip on the SSAF-EXT extends across the entire available rupture area. For the $S = 2.0$ models, a ∼0.5 km separation is enough to stop rupture on the SSAF-EXT from triggering the NF (Figure 6j).

Our simulations with a gap between the SSAF-EXT and the NF suggest that a high-slip San Andreas event (e.g., such that $S = 0.45$) can still trigger slip on the NF, even if the two faults are separated by several kilometers, while the ability of low-stress models (e.g., such that $S = 2.0$) to trigger the NF appears neutralized.

Up to this point, we have observed that, under our current model assumptions, S2N propagating ruptures do not trigger slip on the NF. Furthermore, travel time and slip accumulation north and south of the intersection are probably determining factors in this process. The variable locking depth model highlights an asymmetry in terms of the available SSAF rupture area on either side of the SSAF-NF intersection. This opens a new question on how the locking depth asymmetry could affect the S2N rupture propagation and eventually the triggering of the normal fault. Therefore, we run a simulation with a nucleation location south of the SSAF-NF intersection (Figure 6k). Tractions are such that $S = 0.45$ for both faults. This is the first case we observe triggering of the NF from an S2N propagating rupture. We also tested models where we progressively decreased the NF pre-stress such that $S = 2.0$ (Figure 6l), while keeping the same high pre-stress (such that $S = 0.45$) on the SSAF-EXT. Contrary to the corresponding N2S ruptures (e.g., Figure 6b), we do not observe NF slip.

The introduction of a separation (gap) between the two faults further emphasizes the differences between N2S and S2N scenarios. For $S = 0.45$ on both faults, a ~3 km separation functions as a barrier to NF triggering, while N2S ruptures trigger slip over a 6 km gap (Figure 6c vs. Figure 6n). Finally, an S2N scenario where the NF is pre-stressed obliquely (rake of −45°) does not produce triggering of the NF (Figure 6o). In general, the suite of S2N models exhibit a narrower range of NF-triggering scenarios compared to their N2S counterparts. The reason is the asymmetric disposition of the available rupture area to the north and south of the SSAF-NF intersection. We dedicate the following paragraph to a detailed explanation of this effect.

Figure 7 presents a time snapshot comparison between N2S (Figures 7a–7e) and S2N (Figures 7f–7j) ruptures with variable locking depth. The N2S propagating rupture reproduces observations similar to Figure 4 while the S2N rupture shows a contrasting behavior. The S2N propagating rupture initially produces unfavorable conditions for slip over the available rupture area of the NF, which extends approximately between 0 and 6 km depth (note negative ΔCFS shown with shades of blue in Figures 7f and 7g). After the rupture front passes the NF intersection and slip develops along the northern portion of SSAF-EXT, the negative effect is progressively reversed (Figure 7h) to such a degree that it causes a rupture of the NF (Figures 7i and 7j).

The delayed change to positive ΔCFS leads to a difference in the timing of NF slip triggering between N2S and S2N ruptures. In the N2S case, the appearance of NF-triggered slip coincides with the arrival of the southward propagating rupture front at the SSAF-NF intersection (Figure 7c). On the contrary, in the S2N case, we observe NF-triggered slip several seconds after the rupture front passes the intersection when most of the available fault area north of the intersection has ruptured (Figure 7i).

Finally, due to space limitations, additional discussions and models regarding the effects of pre-stress heterogeneities (resulting from using a reginal stress model) and their impact on the shape of the rupture front and dynamic stress interactions between faults are available in Supporting Information S1 (Figures S8–S10). The same supplementary section also includes a preliminary investigation on how the transitional state of a rupture (subshear to supershear) traveling on the San Andreas and its rupture front shape (e.g., nearly vertical to the intersection) affects the stress interaction with the NF.

4. Normal Fault Dynamic Rake Rotation Imparted by the San Andreas

Previous studies have shown that the slip direction on the fault plane may change with time during dynamic rupture, depending on the magnitude and direction of the initial shear tractions and the heterogeneity of the initial stresses and frictional properties (Bizzarri, 2014; Guatteri & Spudich, 1998; Spudich, 1992). This effect has been observed in events such as the 1986 Mw 6.0 North Palm Springs earthquake (Spudich, 1992), the 1989 Mw 6.9 Loma Prieta earthquake (Guatteri & Cocco, 1996), and the 1995 Kobe earthquake (Yoshida et al., 1996). Geological evidence of rake rotation is generally observed after large earthquakes as curved striations on fault surfaces, known as slickenlines. Such striations have been observed in the 1992 Landers (Johnson et al., 1997), 1995 Kobe (Otsuki et al., 1997), and the 2016 Kaikōura (Kearse et al., 2019) earthquakes.

As discussed in previous sections, San Andreas ruptures interact dynamically with the normal fault under the Salton Sea by perturbing its initial stresses and modulating its slip intensity, direction, and spatial extent. Thus, we examine our final slip models for evidence of rake rotation on the normal fault. The four main factors responsible for the deviation of the rake angle from its initial value are fault-to-fault interaction (including rupture directivity), free surface effects, lateral constraints from the fault edges, and the initial stress level.

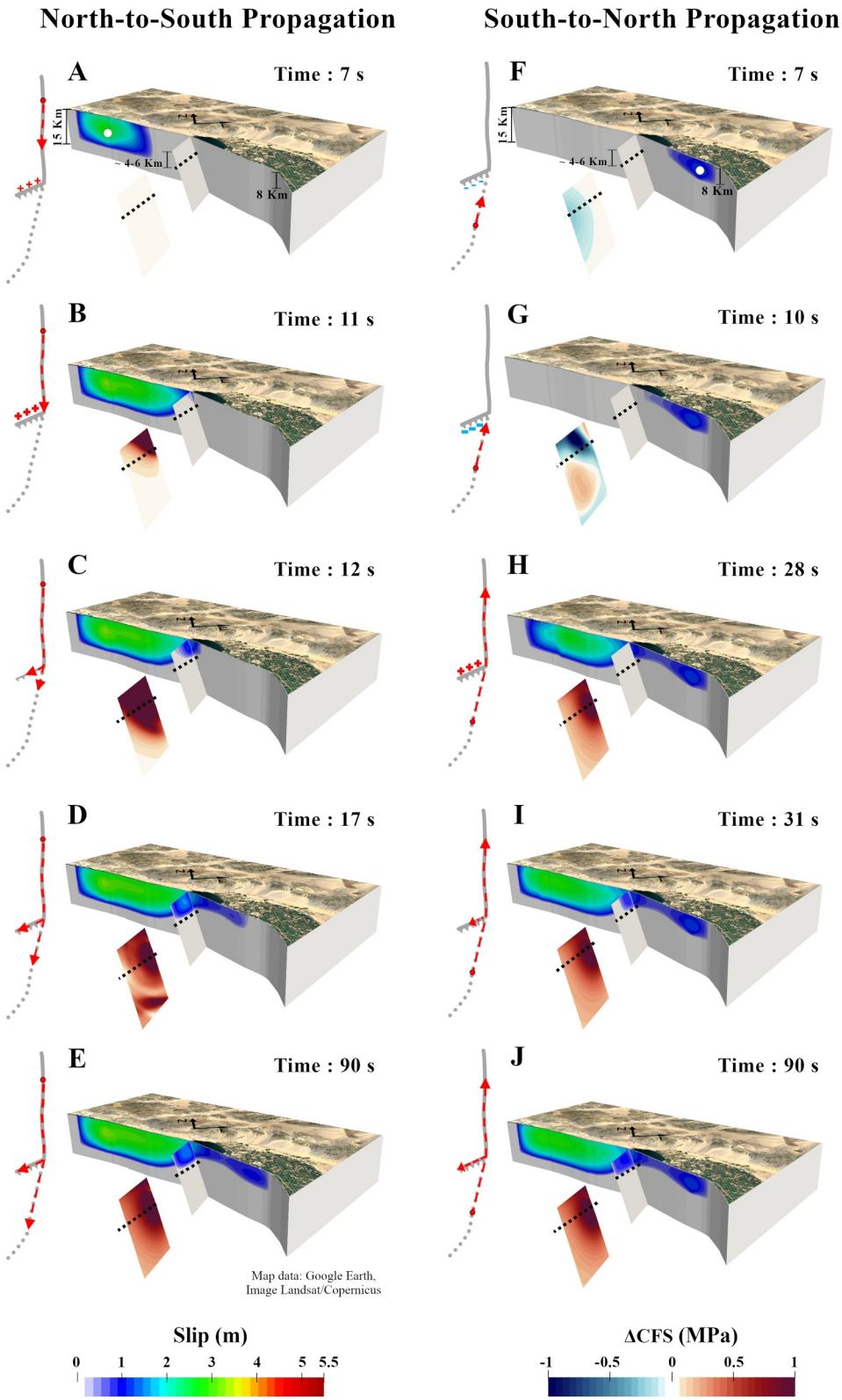

Figure 7.

To gain a first order understanding of this process and identify the different sources of rake rotation we set up four different experiments that include both models with constant and variable locking depth. The results of each experiment are evaluated in comparison to a benchmark rupture (the first column of panels in Figure 8) limited to the NF (the SSAF-EXT does not take part in the simulation), thus limiting rake rotation to that caused exclusively by slip on the NF (see Supporting Information S1 for further details). Tractions are set such that $S = 0.45$ for both faults. The initial stress direction on the NF is set to be consistent with a rake of −90° (pure normal motion) and 180° (right-lateral) for the SSAF-EXT.

In the first experiment, we nucleate an earthquake on the SSAF-EXT (pre-stressed at a rake of 180°) north of the intersection with the NF (N2S propagation). As observed in many cases in Section 3, rupture propagates onto the NF and proceeds south on the SSAF-EXT. In our second experiment, rupture nucleates on the NF and, after a few seconds, passes onto the SSAF-EXT, propagating bilaterally toward the north and south. The third and fourth experiments correspond to simulations with variable locking depth.

Figures 8a–8c highlight the difference in rake rotation between the benchmark rupture limited to the NF and a model with N2S propagation. Fault patches undergoing negligible rake rotation are in white color, while those experiencing more substantial rake rotation appear in shades of blue (for right-lateral motion) or shades of red (for left-lateral motion). In Figure 8a (rupture limited to the NF) the rake angle appears to be unchanged (∼−90°) over most of the NF, with rake variations appearing mostly concentrated around the fault corners at the free surface and the bottom fault edges. The left and right sides of the fault near the free surface show an average rake rotation of about ±15°. In Figure 8b (SSAF-NF joint rupture), most of the NF area is colored blue, indicating normal and right-lateral motion, with rake values of ∼−100° to ∼−115° (the rake rotation is in the opposite direction of the tectonic stress). However, rake rotation increases at the fault corners to max values of ∼+25° and ∼−40° respectively, significantly higher on the NF side near the SSAF-EXT.

Right-lateral motion on the SSAF-EXT north of the intersection with the NF rotates the prestress direction on the NF to values consistent with right-lateral slip. This effect is reversed when rupture passes the NF intersection. The balance of slip magnitude and rupture travel time along the northern and southern portions of the fault determines the direction and magnitude of NF rake rotation. Furthermore, there are other factors that might play a role although difficult (and beyond the scope of this paper) to quantify. For example, the SSAF-EXT fault system is not perfectly symmetric across the NF intersection as the northern portion is ∼10 km longer, nor is it perfectly straight, and thus, separating out each contributing factor is challenging.

Figure 8c highlights rake angle differences of up to 20° between the isolated NF and the compound rupture model, with the highest values concentrated at the SSAF-NF intersection. Differences are lower closer to the free surface, and the midpoint of the fault surface trace rotates about 8°. A comparison between the two experiments reveals that along with rake rotation caused by the free surface and the fault edges, slip on the San Andreas imposes oblique motion on the NF. In our specific case for N2S propagating ruptures, slip on the SSAF rotates the direction of NF coseismic slip to oblique right-lateral values. This contribution is higher at the fault center and decreases toward the fault surface.

In Figure 8e we nucleate an earthquake on the NF, subsequently ruptures pass onto the SSAF-EXT and propagates bilaterally. By comparing Figure 8b with Figure 8e (or alternatively the differences in Figure 8c with Figure 8f), we observe that the experiment with nucleation on the NF generated a weaker rotation (light blue to white colors) in the central portion of the fault. The only difference between the experiments in Figures 8b and 8e is the nucleation location and consequently, the direction of rupture. In the first case (Figure 8b), rupture starts north of

Figure 7. South-to-north (S2N) propagating rupture implementing the variable locking depth triggers slip on the NF. Panels (a–e), left column, show the N2S case while panels (f–j), right column, show the S2N experiment. To highlight the relative position of the rupture front with respect to the SSAF-NF intersection (Bombay Beach) we show time snapshots of fault slip on the San Andreas and the NF. The imparted stress changes are mapped on the NF with a blue (negative ΔCFS) to red (positive ΔCFS) colormap. To facilitate the visualization of stress changes imparted by the SSAF-EXT on the NF, each panel includes a separate view of ΔCFS on the NF next to the fault slip map (detached NF plane). We can clearly see increasing positive ΔCFS values associated with the N2S propagation (panels a and b). When rupture passes the intersection and starts propagating on the NF (panels c and d), the ΔCFS decreases without, however, reaching negative values. On the contrary, the S2N case highlights the initial negative ΔCFS on the NF (panels f and g). When rupture passes the intersection, the ΔCFS transitions progressively from negative to positive (panel h); several seconds later, we observe the triggering of the NF (panels i and j). In the N2S case, we observe NF triggering concurrently with the arrival at the SSAF-NF intersection of the propagating rupture. In contrast, in the S2N case, several seconds have elapsed before we can observe NF slip. The "thinner" locking depth causes a slower propagation to the initial part of the S2N rupture. The black dotted line shows the approximate bottom depth of the NF available rupture area.

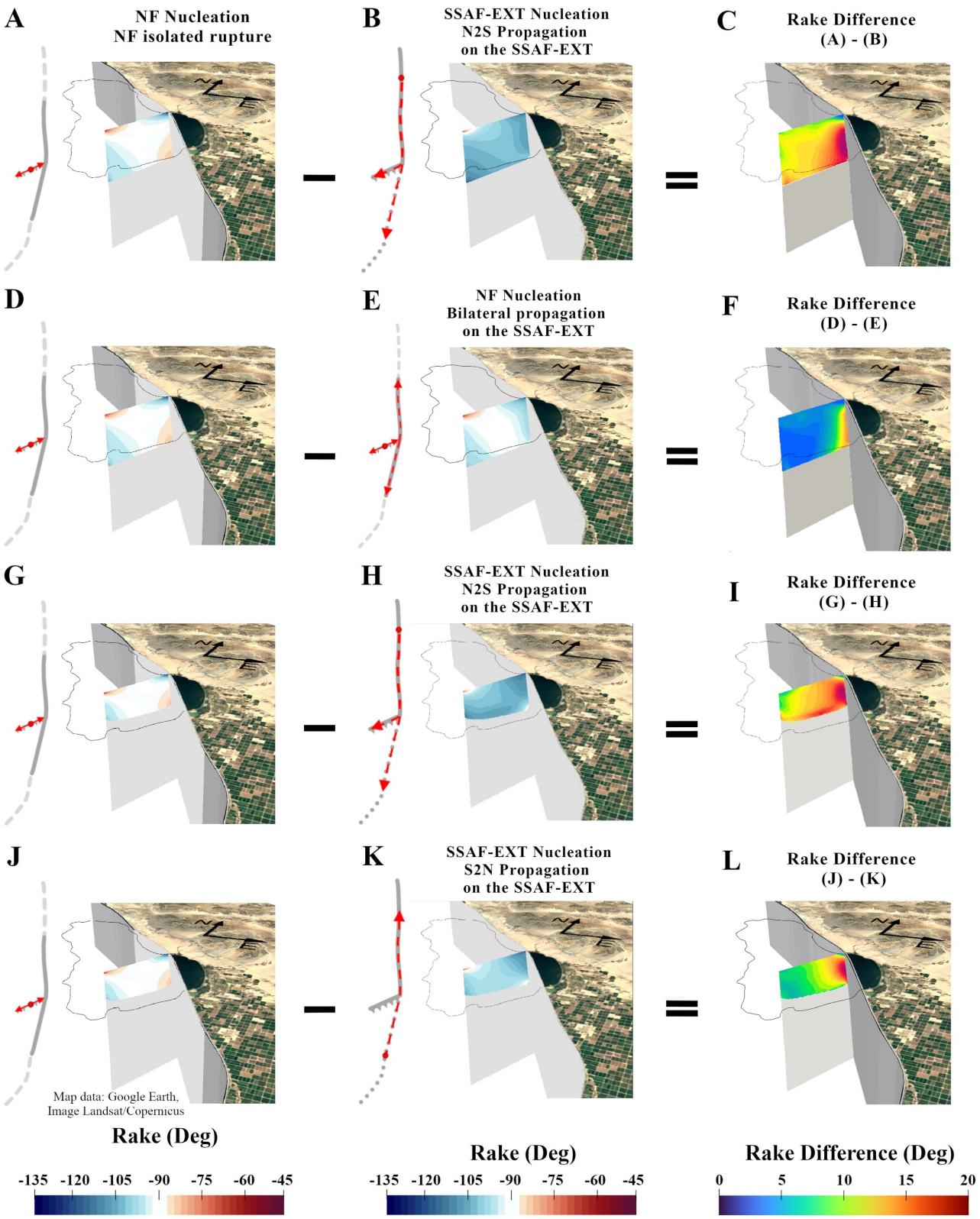

Figure 8.

the intersection (N2S propagation), and consequently, slip occurs first on the northern portion of the fault. Slip on the southern segment occurs only at a later stage. In the second case (Figure 8e), the rupture on the SSAF-EXT is bilateral, and slip occurs almost simultaneously (although there is still some "asymmetry" due to stress changes imparted by the NF rupture) south and north of the intersection. For that reason, slip on the southern portion of the fault "counterbalances" the northern portion, damping eventually the effects from the northern section. We observe the same rake rotation patterns across all our models with joint rupture of the SSAF-NF (or SSAF-EXT-NF).

Figures 8g–8i present rake rotation effects for a variable locking depth model and N2S propagation, while Figures 8j–8l show the S2N counterpart. The variable locking depth experiments reproduce results that are qualitatively and quantitatively comparable to the constant depth models presented in Figures 8a–8f. The S2N case presents a weaker right-lateral rotation (lighter blue colors) than the N2S case. This is expected due to the asymmetry in slip north and south of the intersection in the variable locking depth models.

Due to space limitations, further discussions regarding the effect of the NF initial stress level, a lower NF shear pre-stress amplifies the rake rotation, are presented in Supporting Information S1 (Figure S11).

5. Discussion of Results

Our results help us shed light on which San Andreas rupture scenarios are more likely to trigger slip on the normal fault (e.g., N2S vs. S2N ruptures, oblique vs. normal NF pre-stress), and which are not. For each NF activation scenario, we derive a range of modeled vertical offsets and compare them with values reported for fault H7 in Brothers et al. (2022). Finally, we provide numerical evidence of NF rake rotation imparted by rupture on the San Andreas Fault that might impact the interpretation of the observed and modeled NF vertical offsets.

It is important to note that the variable locking depth models, although more complicated, encompass all the dynamic elements observed in the simpler constant locking depth cases presented in Sections 3.1–3.3. For that reason, they allow a synoptical interpretation of our results without missing key features of the first three sections. To provide a more comprehensive view of our findings, we focus our following discussions on the variable locking depth scenarios and use the constant depth models to support our interpretations as needed.

5.1. Differences Between N2S and S2N Ruptures

The experiments presented in Sections 3.1–3.4 (Figures 3 and 6) demonstrate that N2S ruptures are more likely to trigger NF slip compared to S2N cases. Figure 4 highlights how rupture travel time ahead of and beyond the SSAF-NF intersection, slip pattern, and slip magnitude, are critical in the triggering (or lack thereof) of the NF. Section 5.6 provides further discussions regarding the differences between N2S and S2N ruptures, focusing on the amplitude and range of the modeled vertical displacements. An exception to the above conclusions is a small group of S2N variable locking depth models with high initial shear stress ($S = 0.45$) (Figure 3e vs. Figure 6k), a consequence of the asymmetric slip distribution near the SSAF-NF intersection (Figure 7). These findings underscore the critical role of rupture directionality in the dynamic interplay between the San Andreas and the NF and provide a practical understanding of how major ruptures might propagate through the BSZ. The preferential triggering of NF slip during N2S ruptures results from the stress transfer mechanisms, specifically NF dynamic unclamping, which creates favorable conditions when the San Andreas rupture is north of the SSAF intersection. Although we cannot predict the nucleation location of the next SSAF event neither test the entire spectrum of

Figure 8. Rake rotation on the normal fault imparted by rupture on the San Andreas. The top two rows (panels a–f) show models with constant locking depth (∼14–15 km on the SSAF and 8 km on the NF), while the bottom two rows (panels g–l) show models with variable locking depth. The colormap in panels (a), (b), (d), (e), (g), (h), (j), and (k) represent rake rotation as deviation from the initial shear stress direction consistent with a rake of −90° (normal motion; white color). Blue values indicate a component of right-lateral motion, while red values indicate left-lateral motion. Panels (a, d, g, and j), show the final rake map for the experiments with rupture limited to the NF (no activation of the San Andreas). The concentration of red and blue patches at the left and right corners of the NF is caused by the interaction with the free surface and the constraints posed by the fault edges ("closing" of the fault). Panel (b) shows the experiment with nucleation on the SSAF-EXT and N2S rupture propagation. Panel (c) shows the difference between panel (a) and panel (b). Panel (e) shows the experiment with nucleation on the NF and subsequent bilateral propagation on the SSAF-EXT. Panel (f) shows the difference between panel (d) and panel (e). In panels (b), (e), (h), and (k), in addition to the free surface and edge effects mentioned earlier, the NF rake rotation is mainly a result of stress changes imparted by right-lateral motion on the San Andreas. *Variable locking depth models*: panel (h) shows the final rake map for the experiment with nucleation on the SSAF-EXT and N2S propagation. Panel (i) shows the difference between panel (g) and panel (h). Panel (k) shows the experiment with nucleation on the SSAF-EXT and *S2N propagation*. Panel (l) shows the difference between panel (j) and panel (k). The panels in the left and middle columns include a schematic representation of the rupture propagation and nucleation location.

possible nucleation locations, our results show that vertical displacements observed on the normal faults are more likely to occur for major earthquakes nucleating north of Bombay Beach. In our experiments, and under our current model assumptions, N2S ruptures remain more likely to trigger NF slip even if we move the nucleation location closer to the SSAF-NF intersection (Figure S4 in Supporting Information S1).

5.2. The Variable Locking Depth

The uncertainty regarding the true extent of the seismogenic width (rupture available area) south of Bombay Beach limits our ability to evaluate the likelihood of a sustainable rupture through the BSZ. The most notable effect of these experiments is that S2N ruptures only trigger NF slip (Figure 6k) when a variable locking depth is introduced in our simulation. This is caused by the asymmetric distribution of the available rupture area, which leads to uneven slip, ahead of and beyond the SSAF-NF intersection. This effect is observed only if $S = 0.45$ for both faults and not beyond a 2 km separation. Additionally, the locking depth influences the magnitude of NF slip, with deeper faults (larger along-dip length and thus larger rupture area) producing larger vertical offsets. Our experiments highlight the importance of considering a realistic locking depth, if appropriate, in dynamic rupture modeling, as it could influence the rupture behavior and rupture slip patterns.

5.3. The Effect of Initial NF Shear Stress Direction

As mentioned in Section 1.4, some studies (e.g., Janecke et al., 2011; Jennings & Bryant, 2010; Kirby et al., 2007) suggest that the SSAF and the San Jacinto fault (SJF) are connected by the left-lateral Extra fault (EF), which overlaps with our modeled NF under the Salton Sea (e.g., SCEC CFM v5.3). Our results show that if the NF has a pre-stress direction compatible with a rake of −45° (oblique left-lateral motion) only N2S supershear ($S = 0.45$) ruptures will trigger NF slip. Moreover, changing the orientation of the NF to include a left-lateral component reduces the amount of modeled vertical offsets by ∼35%. For example, the NF vertical offset in the model with $S = 0.45$ in both faults drops from 1.17 m (Figure 6a) to ∼0.7 m (Figure 6e) in the oblique pre-stress case (a reduction of ∼38%), underpredicting the maximum vertical offset values reported by Brothers et al. (2022). A smaller but significant reduction of ∼30% occurs in the corresponding constant locking depth model (e.g., Figure 3f vs. Figure 5c). A purely left-lateral NF pre-stress further neutralizes the ability of the San Andreas to trigger NF slip (Figure 6e vs. Figure 6g). The right-lateral stress imparted by the San Andreas reduces the amplitude of the initial shear stress on the NF, making it less favorable to rupture and producing smaller amounts of slip. S2N ruptures with an oblique or left-lateral NF (not shown here) do not trigger slip on the NF. Our results have important implications for understanding fault kinematics under the Salton Sea. If the NF exhibits oblique rather than purely normal faulting, the potential of SSAF ruptures triggering NF slip decreases. This points to the need for further investigation into the kinematics of the network of normal faults under the Salton Sea.

5.4. Separation Between the Two Faults

High-stress N2S ruptures on the San Andreas, with both normal and oblique NF pre-stress, can trigger slip on the NF even if the two faults are separated by several kilometers (Figures 6c and 6d) and consequently displace the stratigraphic layers. Alternatively, assuming that the NF is a continuous 10–15 km along strike structure, the San Andreas could push to rupture small and isolated (∼6 km from the SSAF) asperities on the NF. Lower stress N2S models with a gap appear to not produce NF slip (Figure 6j). It is also important to note that the existence of a separation between the two faults further reduces the likelihood of S2N ruptures triggering NF slip. Indeed, the maximum gap over which an S2N rupture appears to trigger the NF is 2 km as opposed to 6 km for the N2S scenarios. These observations for the N2S high-stress ($S = 0.45$) models have broader implications for seismic hazard assessment in regions with complex fault networks. They suggest that slip triggering can occur over gaps of several kilometers and that smaller splay faults, not necessarily connected to the main fault, can record evidence of past larger events.

5.5. Dynamic Rake Rotation

Dynamic rake rotation might interfere with the ability of the SSAF to trigger slip on the NF as well as the amount of observed subsidence. We found that San Andreas ruptures cause NF rake rotation, imparted through dynamic stress changes (Figure 8). For models with $S = 0.45$ on both faults and N2S propagation, we quantified the rotation to be ∼8° near the midpoint of the NF surface trace and increases toward the SSAF-NF intersection to

15°–20°. The central and deeper portion of the fault also experiences higher (right-lateral) rotation with respect to the free surface. For that reason, depending on how close to the San Andreas we collect our NF observations, an estimation of rake rotation might be useful information. Simulations with lower NF pre-stress (e.g., such that $S = 3.0$) produce an additional increase of rake rotation of up to 20° (Figure S11 in Supporting Information S1).

5.6. Modeled Vertical Offsets

The suite of high stress ($S = 0.45$ on both faults) N2S ruptures show a range variability of vertical offsets (subsidence) between approximately 0.2 and 1.2 m, close to the 0.2–1.4 m range reported by Brothers et al. (2022). Although there is no unique model to explain the full spectrum of observations, it appears that models with NF oblique motion are required to reproduce the lower part of the displacement range and models with NF normal motion do a better job in reproducing the higher values. Therefore, the range variability of vertical offsets reported by Brothers et al. (2022), could be explained solely by the N2S high-stress cases. It is noteworthy how NF oblique motion is an efficient mechanism for reducing NF vertical offsets and how the San Andreas can trigger slip on small, isolated asperities. The average NF vertical offset of all our simulations with $S = 0.45$ and N2S propagation is ∼0.7 m. Note that the maximum value of vertical displacement increases to ∼1.7 m for the constant depth locking models, a consequence of a deeper NF locking depth of 8 km (larger rupture area).

Although less likely, NF triggering by S2N San Andreas ruptures can also occur in the variable locking depth models. Indeed, models with oblique NF initial shear stress (Figure 6e vs. Figure 6o) or models with gaps (Figure 6c vs. Figure 6m) show that NF triggering by S2N ruptures occurs within a more limited range of initial conditions and geometric configurations compared to N2S cases. When S2N ruptures trigger the NF, the modeled vertical offsets range from ∼0.7 to ∼0.8 m, which is considerably narrower than the range produced in the N2S cases. Thus, it appears that N2S propagating ruptures could trigger a wider range of modeled vertical offsets compared to the S2N counterpart. Lower stress ($S = 2.0$) variable locking depth models are significantly less efficient in triggering NF slip and, for that reason, fail to reproduce a range of modeled values comparable to the stratigraphic observations (Figures 6h–6j).

5.7. Rupture Scenarios That Do Not Trigger the NF

Rupture scenarios that do not trigger the NF or produce negligible amounts of NF slip also contribute to a better understanding of the interactions between the two faults and the seismic hazard in this area. For that reason, we should be aware that major earthquakes on the SSAF might not always trigger slip on the NF and thus undetectable when interpreting stratigraphic sections. These include a variety of N2S scenarios with low stress (such that $S = 2.0$) on both faults, including models with small gaps greater than 0.5 km (e.g., Figure 6j), S2N propagating ruptures with low NF pre-stress (such that $S \geq 2.0$; e.g., Figure 6l), high stress S2N propagating ruptures with fault separation equal or greater than 3 km (e.g., Figure 6n) or oblique NF pre-stress (Figure 6o), and the less plausible scenarios with pure left-lateral motion on the NF. Some events might be undetectable from the seismic reflection profiles due to the limited along-strike extension of coseismic slip (Figure 6i) and closer to the San Andreas or because they occur on fault asperities placed diametrically from the SSAF-NF intersection (Figure 6d).

6. Limitations of Our Work

Modeling earthquakes in the BSZ is challenging due to its complexity, and some assumptions and simplifications must be made. Our understanding of the possible connection between the SSAF and the IF within the southern BSZ and their relation to smaller structures (e.g., cross-faults) is limited due to the lack of surface expression of the SSAF as well as other faults. The precise direction in which the SSAF extends south of Bombay Beach could impact the behavior of dynamic ruptures nucleating to the south of the SSAF-NF intersection as well as ruptures approaching from the north. However, the lineament of seismicity projecting immediately south of Bombay Beach and into the Salton Sea (e.g., see Figure 4 in Hauksson et al. (2022)) suggests that our geometry wouldn't change for at least 10 km from the SSAF-NF intersection. Generally, for kinematic and numerical models (e.g., Dorsett et al., 2019; Kyriakopoulos et al., 2019), the SSAF in the BSZ is typically projected along two distinct paths, which are inferred from seismic activity (Hauksson et al., 2022; Lin et al., 2007) and other geologic considerations. Predicting the dynamic rupture behavior with a different fault geometry and without running new models can be challenging, if not impossible. If the southward projection of the SSAF-EXT is sharper than in our current model, it could make triggering the NF more or less likely. Nevertheless, our general observation that

ruptures approaching the NF from the south would produce clamping, thus inhibiting NF slip, is still valid. Additionally, even if the geometry is slightly different south of the intersection, the dynamic considerations regarding N2S ruptures remain the same.

Similarly, the connectivity between smaller faults in the BSZ is crucial for accurate seismic modeling and hazard assessment. It may be tempting to link onshore faults, such as the EF and the ERF, with the offshore network of normal faults in the Salton Sea. However, current evidence cannot confirm these connections (Brothers et al., 2009; Dorsett et al., 2019; Hudnut, Seeber, & Pacheco, 1989; Nicholson et al., 1986), and for this reason, we focused on the best representative fault from the network (fault H7; Brothers et al., 2009, 2022), considering it independent from other faults. If these normal faults are indeed connected to larger onshore faults, new simulations would be required to accurately model earthquake behavior. This information could also improve our understanding of the pre-stress direction (purely normal vs. oblique) on the faults under the Salton Sea, leading to better estimates of the vertical NF offsets triggered by ruptures along the SSAF.

Another debatable topic is the dip of the SSAF north of the fault intersection. There is incremental evidence during the last years that the fault dips to the NE with an average dip angle of 60°–80° from Bombay Beach to Thousand Palms (e.g., Langenheim & Fuis, 2022; Vavra et al., 2023). Since a final consensus on the SSAF structure is still lacking (with the new SCEC Community Fault Model v6.1 having a "preferred" dip of ∼60° but an alternative dip of 90°), for simplicity, we use a 90° dip on the SSAF. The next modeling phase would be designed to test for fault dip variations and probably include a propeller-like SSAF structure, which would be required to connect the SSAF to its southward extension. Simulations with a dipping SSAF would alter the stress radiation pattern and intensity, potentially leading to different dynamic interactions between the two faults. However, we also expect the dynamic clamping-unclamping mechanism imparted on the normal fault by the San Andreas, which plays a dominant role in activating the normal fault, to still occur even with a dipping SSAF. Such behavior is the subject of future work.

A consequence of the finite size of our computational domain is that San Andreas events cannot propagate beyond the domain's northwest and southeast boundaries. A real earthquake could propagate further (e.g., beyond our current model boundaries), potentially triggering the NF given the favorable conditions of rupture north of the intersection with the NF. Part of our conclusions depend on the specific characteristics of the variable locking depth model under the Salton Sea and the northern BSZ. However, the general results likely do not depend strongly on the fine details.

Our dynamic rupture simulations help us understand first-order components of coseismic fault interaction and, thus, determine under which conditions the San Andreas might trigger slip on the NF. We are aware that other processes not considered in this work, such as poroelastic relaxation and aseismic motion (e.g., Chen & Shearer, 2011; Im & Avouac, 2021; Lohman & McGuire, 2007; Roland & McGuire, 2009; Sirorattanakul et al., 2022; Vidale & Shearer, 2006), as well as effects related to the geothermal field production in the BSZ (Barbour et al., 2016), may alter the stresses on our faults and induce additional deformation (Lohman & McGuire, 2007) and delayed triggering (Hudnut, Seeber, & Pacheco, 1989; Magistrale et al., 1989; Ross et al., 2019; Sharp et al., 1989). We should also note that aseismic motion and delayed triggering are not resolvable from the stratigraphic record, making their implementation even more challenging.

7. Conclusions

Based on our current modeling assumptions, it is very likely that major earthquakes on the SSAF, especially North-to-South (N2S) propagating ruptures, trigger slip on the normal faults under the Salton Sea. Using realistic fault geometry, locking depth, initial stress, and frictional parameters, the triggered slip causes normal fault (NF) vertical offsets comparable to seismic stratigraphic interpretations from Brothers et al. (2022). South-to-North (S2N) ruptures appear to be less likely to trigger normal fault slip, although our simulations show that we cannot exclude this possibility. Furthermore, in a more limited number of cases, the SSAF could rupture without triggering the NF or without producing discernible amounts of NF slip, which could render some of these events undetectable within the stratigraphic record of the NF. In addition, because we have no absolute certainty that the San Andreas continues south of the bottom edge of the Salton Sea, S2N ruptures remain enigmatic and challenging to model. A similar argument is valid regarding the seismogenic width, a critical parameter for sustainable ruptures through this area. Finally, our models suggest that San Andreas ruptures impart right-lateral coseismic rake rotation on the normal fault, potentially affecting the interpretation of the source mechanism of slip episodes

in the stratigraphic record. Our simulations produce normal fault rake rotation near the free surface (~8°) that, depending on the initial conditions, can reach max values of up to ~20° in the center of the fault and up to ~35° near the intersection with the San Andreas. In conclusion, our dynamic rupture scenarios highlight key factors influencing the coseismic interaction between the SSAF and NF.

Data Availability Statement

The authors did not use external data sets nor collect or produce new data sets. The mesh generator software Trelis 17.0, used to build the meshes, can be purchased from Coreform LLC (https://coreform.com). The dynamic rupture code FaultMod, used to run the simulations, is publicly available at https://code.usgs.gov/esc/faultmod. The visualization software ParaView, used to display the results, is publicly available at https://paraview.org. The GNU Image Manipulation Program v2.10 (GIMP), used to create the schematic figures, is publicly available at https://www.gimp.org/. The data files and scripts used to produce the results presented in this work are publicly available (Bazán Flores, 2024).

Acknowledgments
This work was funded by the Southern California Earthquake Center (SCEC) through Award #22153. SCEC is funded by the NSF EAR-1033462 & USGS G12AC20038. Figures showing dynamic rupture results were made using ParaView (Ahrens et al., 2005). The Google Earth map visible in Figures 2–8 is from Landsat/Copernicus. Figure 1 was generated using GMT (Wessel et al., 2019). We use the GNU Image Manipulation Program GIMP v2.10 (https://www.gimp.org/) to merge the figures created in ParaView. The authors are grateful for their comments to Ruth Harris (USGS), two anonymous reviewers, and the editor, who significantly improved this paper. The authors would also like to thank Michael Barall (USGS) for his continuous support with FaultMod. Any use of trade, firm, or product names is for descriptive purposes only and does not imply endorsement by the U.S. Government.

References

Ahrens, J., Geveci, B., & Law, C. (2005). ParaView: An end-user tool for large-data visualization. In C. D. Hansen, & C. R. Johnson (Eds.), *Visualization handbook* (pp. 717–731). https://doi.org/10.1016/B978-012387582-2/50038-1

Andrews, D. J. (1976). Rupture velocity of plane strain shear cracks. *Journal of Geophysical Research*, *81*(32), 5679–5687. https://doi.org/10.1029/JB081i032p05679

Archuleta, R. J. (1984). A faulting model for the 1979 Imperial Valley earthquake. *Journal of Geophysical Research*, *89*(B6), 4559–4585. https://doi.org/10.1029/jb089ib06p04559

Barall, M. (2009). A grid-doubling finite-element technique for calculating dynamic three-dimensional spontaneous rupture on an earthquake fault. *Geophysical Journal International*, *178*(2), 845–859. https://doi.org/10.1111/j.1365-246X.2009.04190.x

Barbour, A. J., Evans, E. L., Hickman, S. H., & Eneva, M. (2016). Subsidence rates at the southern Salton Sea consistent with reservoir depletion. *Journal of Geophysical Research: Solid Earth*, *121*(7), 5308–5327. https://doi.org/10.1002/2016JB012903

Bazán Flores, L. I. (2024). Numerical results for Bazán Flores et al., 2024. (JGR Accepted) (version 3) [Dataset]. In *Journal of Geophysical Research Solid Earth*. Zenodo. https://doi.org/10.5281/zenodo.13952792

Biasi, G. P., & Scharer, K. M. (2019). The current unlikely earthquake Hiatus at California's transform boundary paleoseismic sites. *Seismological Research Letters*, *90*(3), 1168–1176. https://doi.org/10.1785/0220180244

Bizzarri, A. (2014). Rake rotation introduces ambiguity in the formulation of slip-dependent constitutive models: Slip modulus or slip path? *Annals of Geophysics*, *57*(5). https://doi.org/10.4401/ag-6582

Brodsky, E. E., & Lajoie, L. J. (2013). Anthropogenic seismicity rates and operational parameters at the Salton Sea geothermal field. *Science*, *341*(6145), 543–546. https://doi.org/10.1126/science.1239213

Brothers, D. S., Driscoll, N. W., Kent, G. M., Baskin, R. L., Harding, A. J., & Kell, A. M. (2022). Seismostratigraphic analysis of Lake Cahuilla sedimentation cycles and fault displacement history beneath the Salton Sea, California, USA. *Geosphere*, *18*(4), 1354–1376. https://doi.org/10.1130/GES02468.1

Brothers, D. S., Driscoll, N. W., Kent, G. M., Harding, A. J., Babcock, J. M., & Baskin, R. L. (2009). Tectonic evolution of the Salton Sea inferred from seismic reflection data. *Nature Geoscience*, *2*(8), 581–584. https://doi.org/10.1038/ngeo590

Brothers, D. S., Kilb, D., Luttrell, K., Driscoll, N. W., & Kent, G. M. (2011). Loading of the San Andreas Fault by flood-induced rupture of faults beneath the Salton Sea. *Nature Geoscience*, *4*(7), 486–492. https://doi.org/10.1038/ngeo1184

Chen, X., & Shearer, P. M. (2011). Comprehensive analysis of earthquake source spectra and swarms in the Salton Trough, California. *Journal of Geophysical Research*, *116*(B9), B09309. https://doi.org/10.1029/2011JB008263

Crowell, B. W., Bock, Y., Sandwell, D. T., & Fialko, Y. (2013). Geodetic investigation into the deformation of the Salton Trough. *Journal of Geophysical Research: Solid Earth*, *118*(9), 5030–5039. https://doi.org/10.1002/JGRB.50347

Day, S. M. (1982). Three-dimensional simulation of spontaneous rupture: The effect of nonuniform prestress. *Bulletin of the Seismological Society of America*, *72*(6A), 1881–1902. https://doi.org/10.1785/BSSA07206A188

DeDontney, N., Rice, J. R., & Dmowska, R. (2012). Finite element modeling of branched ruptures including off-fault plasticity. *Bulletin of the Seismological Society of America*, *102*(2), 541–562. https://doi.org/10.1785/0120110134

Di Toro, G., Han, R., Hirose, T., De Paola, N., Nielsen, S., Mizoguchi, K., et al. (2011). Fault lubrication during earthquakes. *Nature*, *471*(7339), 494–498. https://doi.org/10.1038/nature09838

Dorsett, J. H., Madden, E. H., Marshall, S. T., & Cooke, M. L. (2019). Mechanical models suggest fault linkage through the Imperial Valley, California, U.S.A. *Bulletin of the Seismological Society of America*, *109*(4), 1217–1234. https://doi.org/10.1785/0120180303

Elders, W. A., Rex, R. W., Meidav, T., Robinson, P. T., & Biehler, S. (1972). Crustal spreading in southern California. *Science*, *178*(4056), 15–24. https://doi.org/10.1126/science.178.4056.15

Fialko, Y. (2006). Interseismic strain accumulation and the earthquake potential on the Southern San Andreas Fault system. *Nature*, *441*(7096), 968–971. https://doi.org/10.1038/nature04797

Field, E. H., Arrowsmith, R. J., Biasi, G. P., Bird, P., Dawson, T. E., Felzer, K. R., et al. (2014). Uniform California Earthquake Rupture Forecast, version 3 (UCERF3)—The time-independent model. *Bulletin of the Seismological Society of America*, *104*(3), 1122–1180. https://doi.org/10.1785/0120130164

Fuis, G. S., Mooney, W. D., Healy, J. H., McMechan, G. A., & Lutter, W. J. (1984). A seismic refraction survey of the Imperial Valley Region, California. *Journal of Geophysical Research*, *89*(B2), 1165–1189. https://doi.org/10.1029/JB089IB02P01165

Guatteri, M., & Cocco, M. (1996). On the variation of slip direction during earthquake rupture: Supporting and conflicting evidence from the 1989 Loma Prieta earthquake. *Bulletin of the Seismological Society of America*, *86*(6), 1935–1943. https://doi.org/10.1785/bssa0860061935

Guatteri, M., & Spudich, P. (1998). Coseismic temporal changes of slip direction: The effect of absolute stress on dynamic rupture. *Bulletin of the Seismological Society of America*, *88*(3), 777–789. https://doi.org/10.1785/bssa0880030777

Han, L., Hole, J. A., Stock, J. M., Fuis, G. S., Kell, A., Driscoll, N. W., et al. (2016). Continental rupture and the creation of new crust in the Salton Trough rift, southern California and northern Mexico: Results from the Salton Seismic Imaging Project. *Journal of Geophysical Research: Solid Earth*, *121*(10), 7469–7489. https://doi.org/10.1002/2016JB013139

Hardebeck, J. L., & Shearer, P. M. (2003). Using S/P amplitude ratios to constrain the focal mechanisms of small earthquakes. *Bulletin of the Seismological Society of America*, *93*(6), 2434–2444. https://doi.org/10.1785/0120020236

Harris, R., & Simpson, R. (1992). Changes in static stress on southern California faults after the 1992 Landers earthquake. *Nature*, *360*(6401), 251–254. https://doi.org/10.1038/360251a0

Harris, R. A., Aagaard, B., Barall, M., Ma, S., Roten, D., Olsen, K., et al. (2018). A suite of exercises for verifying dynamic earthquake rupture codes. *Seismological Research Letters*, *89*(3), 1146–1162. https://doi.org/10.1785/0220170222

Harris, R. A., Barall, M., Archuleta, R., Dunham, E., Aagaard, B., Ampuero, J. P., et al. (2009). The SCEC/USGS dynamic earthquake rupture code verification exercise. *Seismological Research Letters*, *80*(1), 119–126. https://doi.org/10.1785/gssrl.80.1.119

Hauksson, E. (2000). Crustal structure and seismicity distribution adjacent to the Pacific and North America plate boundary in southern California. *Journal of Geophysical Research*, *105*(B6), 13875–13903. https://doi.org/10.1029/2000jb900016

Hauksson, E., Meier, M. A., Ross, Z. E., & Jones, L. M. (2017). Evolution of seismicity near the southernmost terminus of the San Andreas Fault: Implications of recent earthquake clusters for earthquake risk in southern California. *Geophysical Research Letters*, *44*(3), 1293–1301. https://doi.org/10.1002/2016GL072026

Hauksson, E., Stock, J. M., & Husker, A. L. (2022). Seismicity in a weak crust: The transtensional tectonics of the Brawley Seismic Zone section of the Pacific–North America plate boundary in southern California, USA. *Geophysical Journal International*, *231*(1), 717–735. https://doi.org/10.1093/gji/ggac205

Hauksson, E., Yang, W., & Shearer, P. M. (2012). Waveform relocated earthquake catalog for southern California (1981 to June 2011). *Bulletin of the Seismological Society of America*, *102*(5), 2239–2244. https://doi.org/10.1785/0120120010

Hill, R. G., Weingarten, M., Rockwell, T. K., & Fialko, Y. (2023). Major southern San Andreas earthquakes modulated by lake-filling events. *Nature*, *618*(7966), 761–766. https://doi.org/10.1038/s41586-023-06058-9

Hudnut, K., Seeber, L., Rockwell, T., Goodmacher, J., Klinger, R., Lindvall, S., & McElwain, R. (1989). Surface ruptures on cross-faults in the 24 November 1987 Superstition Hills, California, earthquake sequence. *Bulletin of the Seismological Society of America*, *79*(2), 282–296.

Hudnut, K. W., Seeber, L., & Pacheco, J. (1989). Cross-fault triggering in the November 1987 Superstition Hills Earthquake Sequence, southern California. *Geophysical Research Letters*, *16*(2), 199–202. https://doi.org/10.1029/GL016I002P00199

Hudnut, K. W., Seeber, L., & Rockwell, T. (1989). Slip on the Elmore Ranch fault during the past 330 years and its relation to slip on the Superstition Hills fault. *Bulletin of the Seismological Society of America*, *79*(2), 330–341. https://doi.org/10.1785/BSSA0790020330

Ida, Y. (1972). Cohesive force across the tip of a longitudinal-shear crack and Griffith's specific surface energy. *Journal of Geophysical Research*, *77*(20), 3796–3805. https://doi.org/10.1029/jb077i020p03796

Im, K., & Avouac, J. P. (2021). On the role of thermal stress and fluid pressure in triggering seismic and aseismic faulting at the Brawley Geothermal Field, California. *Geothermics*, *97*, 102238. https://doi.org/10.1016/j.geothermics.2021.102238

Janecke, S. U., Dorsey, R. J., Forand, D., Steely, A. N., Kirby, S. M., Lutz, A. T., et al. (2011). High geologic slip rates since early Pleistocene initiation of the San Jacinto and San Felipe Fault zones in the San Andreas Fault system: Southern California, USA. *Special Papers—Geological Society of America*, *475*. https://doi.org/10.1130/2010.2475

Jennings, C., & Bryant, W. (2010). Fault activity map of California. California Geologic Data Map No. 6, scale 1:750,000.

Johnson, A. M., Fleming, R. W., Cruikshank, K. M., Martosudarmo, S. Y., Johnson, N. A., Johnson, K. M., & Wei, W. (1997). *Analecta of structures formed during the 28 June 1992 Landers-Big Bear, California, earthquake sequence*. U.S. Geological Survey Open-File Report, 97–94.

Johnson, C. E., & Hadley, D. M. (1976). Tectonic implications of the Brawley earthquake swarm, Imperial Valley, California, January 1975. *Bulletin of the Seismological Society of America*, *66*(4), 1133–1144. https://doi.org/10.1785/BSSA0660041133

Kearse, J., Kaneko, Y., Little, T., & Van Dissen, R. (2019). Curved slickenlines preserve direction of rupture propagation. *Geology*, *47*(9), 838–842. https://doi.org/10.1130/G46563.1

King, G. C. P., Stein, R. S., & Lin, J. (1994). Static stress changes and the triggering of earthquakes. *Bulletin of the Seismological Society of America*, *84*(3), 935–953.

Kirby, S. M., Janecke, S. U., Dorsey, R. J., Housen, B. A., Langenheim, V. E., McDougall, K. A., & Steeley, A. N. (2007). Pleistocene Brawley and Ocotillo Formations: Evidence for initial strike-slip deformation along the San Felipe and San Jacinto fault zones, southern California. *The Journal of Geology*, *115*(1), 43–62. https://doi.org/10.1086/509248

Kyriakopoulos, C., & Oglesby, D. (2024). Direct dynamic triggering scenarios of the Southern San Andreas Fault by Moderate-Magnitude Cross-Fault Earthquakes in the Brawley Seismic Zone, California. *Seismological Research Letters*, *95*(5), 2859–2873. https://doi.org/10.1785/0220230326

Kyriakopoulos, C., Oglesby, D. D., Rockwell, T. K., Meltzner, A. J., Barall, M., Fletcher, J. M., & Tulanowski, D. (2019). Dynamic rupture scenarios in the Brawley Seismic Zone, Salton Trough, Southern California. *Journal of Geophysical Research: Solid Earth*, *124*(4), 3680–3707. https://doi.org/10.1029/2018JB016795

Langenheim, V. E., & Fuis, G. S. (2022). Insights into the geometry and evolution of the Southern San Andreas Fault from geophysical data, southern California. *Geosphere*, *18*(2), 615–638. https://doi.org/10.1130/GES02378.1

Larsen, S., & Reilinger, R. (1991). Age constraints for the present fault configuration in the Imperial Valley, California: Evidence for northwestward propagation of the Gulf of California rift system. *Journal of Geophysical Research*, *96*(B6), 10339–10352. https://doi.org/10.1029/91jb00618

Lin, G., Shearer, P. M., & Hauksson, E. (2007). Applying a three-dimensional velocity model, waveform cross correlation, and cluster analysis to locate southern California seismicity from 1981 to 2005. *Journal of Geophysical Research*, *112*(B12), B12309. https://doi.org/10.1029/2007JB004986

Lin, J., & Stein, R. S. (2004). Stress triggering in thrust and subduction earthquakes and stress interaction between the southern San Andreas and nearby thrust and strike-slip faults. *Journal of Geophysical Research*, *109*(B2), B02303. https://doi.org/10.1029/2003jb002607

Lohman, R. B., & McGuire, J. J. (2007). Earthquake swarms driven by aseismic creep in the Salton Trough, California. *Journal of Geophysical Research*, *112*(B4), B04405. https://doi.org/10.1029/2006JB004596

Magistrale, H., Jones, L., & Kanamori, H. (1989). The Superstition Hills, California, earthquakes of 24 November 1987. *Bulletin of the Seismological Society of America*, *79*(2), 239–251. https://doi.org/10.1785/bssa0790020239

Nazareth, J. J., & Hauksson, E. (2004). The seismogenic thickness of the southern California crust. *Bulletin of the Seismological Society of America*, *94*(3), 940–960. https://doi.org/10.1785/0120020129

Newmark, R. L., Kasameyer, P. W., & Younker, L. W. (1988). Preliminary report on shallow research drilling in the Salton Sea region. *Office of Scientific & Technical Information Report*. https://doi.org/10.2172/6662746

Nicholson, C., & Seeber, L. (1989). Evidence for contemporary block rotation in strike-slip environments: Examples from the San Andreas Fault system, southern California. In C. Kissel, & C. Laj (Eds.), *Paleomagnetic rotations and continental deformation* (Vol. 254, pp. 257–277). Springer. https://doi.org/10.1007/978-94-009-0869-7_16

Nicholson, C., Seeber, L., Williams, P., & Sykes, L. R. (1986). Seismic evidence for conjugate slip and block rotation within the San Andreas Fault System, southern California. *Tectonics*, *5*(4), 629–648. https://doi.org/10.1029/TC005i004p00629

Otsuki, K., Minagawa, J., Aono, M., & Ohtake, M. (1997). On the curved striations of Nojima Seismic Fault engraved at the 1995 Hyogoken-Nambu Earthquake, Japan. *Zisin (Journal of the Seismological Society of Japan. 2nd Ser.)*, *49*(4), 451–461. https://doi.org/10.4294/zisin1948.49.4_451

Persaud, P., Ma, Y., Stock, J. M., Hole, J. A., Fuis, G. S., & Han, L. (2016). Fault zone characteristics and basin complexity in the southern Salton Trough, California. *Geology*, *44*(9), 747–750. https://doi.org/10.1130/G38033.1

Philibosian, B., Fumal, T., & Weldon, R. (2011). San Andreas Fault earthquake chronology and Lake Cahuilla History at Coachella, California. *Bulletin of the Seismological Society of America*, *101*(1), 13–38. https://doi.org/10.1785/0120100050

Plesch, A., Shaw, J. H., Benson, C., Bryant, W. A., Carena, S., Cooke, M. L., et al. (2007). Community Fault Model (CFM5.0) for southern California. *Bulletin of the Seismological Society of America*, *97*(6), 1793–1802. https://doi.org/10.1785/0120050211

Rice, J. R. (1993). Spatio-temporal complexity of slip on a fault. *Journal of Geophysical Research*, *98*(B6), 9885–9907. https://doi.org/10.1029/93JB00191

Rockwell, T. K., Meltzner, A. J., & Haaker, E. C. (2018). Dates of the two most recent surface ruptures on the southernmost San Andreas Fault recalculated by precise dating of Lake Cahuilla dry periods. *Bulletin of the Seismological Society of America*, *108*(5), 2634–2649. https://doi.org/10.1785/0120170392

Rockwell, T. K., Meltzner, A. J., Haaker, E. C., & Madugo, D. (2022). The late Holocene history of Lake Cahuilla: Two thousand years of repeated fillings within the Salton Trough, Imperial Valley, California. *Quaternary Science Reviews*, *282*, 107456. https://doi.org/10.1016/j.quascirev.2022.107456

Roland, E., & McGuire, J. J. (2009). Earthquake swarms on transform faults. *Geophysical Journal International*, *178*(3), 1677–1690. https://doi.org/10.1111/j.1365-246X.2009.04214.x

Ross, J. E. (2020). Formation of California's Salton Sea in 1905–07 was not "accidental". In D. M. Miller (Ed.), *Changing facies: The 2020 desert symposium field guide and proceedings* (pp. 217–230). Desert Symposium, Inc. Retrieved from http://www.desertsymposium.org/History.html

Ross, Z. E., Idini, B., Jia, Z., Stephenson, O. L., Zhong, M., Wang, X., et al. (2019). Hierarchical interlocked orthogonal faulting in the 2019 Ridgecrest earthquake sequence. *Science*, *366*(6463), 346–351. https://doi.org/10.1126/science.aaz0109

Sahakian, V., Kell, A., Harding, A., Driscoll, N., & Kent, G. (2016). Geophysical evidence for a San Andreas subparallel transtensional fault along the northeastern shore of the Salton Sea. *Bulletin of the Seismological Society of America*, *106*(5), 2067–2079. https://doi.org/10.1785/0120150350

Schmitt, A. K., & Vazquez, J. A. (2006). Alteration and remelting of nascent oceanic crust during continental rupture: Evidence from zircon geochemistry of rhyolites and xenoliths from the Salton Trough, California. *Earth and Planetary Science Letters*, *252*(3–4), 260–274. https://doi.org/10.1016/j.epsl.2006.09.041

Sharp, R. V., Budding, K. E., Boatwright, J., Ader, M. J., Bonilla, M. G., Clark, M. M., et al. (1989). Surface faulting along the Superstition Hills fault zone and nearby faults associated with the earthquakes of 24 November 1987. *Bulletin of the Seismological Society of America*, *79*(2), 252–281. https://doi.org/10.1785/bssa0790020252

Sirorattanakul, K., Ross, Z. E., Khoshmanesh, M., Cochran, E. S., Acosta, M., & Avouac, J.-P. (2022). The 2020 Westmorland, California earthquake swarm as aftershocks of a slow slip event sustained by fluid flow. *Journal of Geophysical Research: Solid Earth*, *127*(11), e2022JB024693. https://doi.org/10.1029/2022JB024693

Smith-Konter, B. R., Sandwell, D. T., & Shearer, P. (2011). Locking depths estimated from geodesy and seismology along the San Andreas Fault System: Implications for seismic moment release. *Journal of Geophysical Research*, *116*(6), B06401. https://doi.org/10.1029/2010JB008117

Spudich, P. K. P. (1992). On the inference of absolute stress levels from seismic radiation. *Tectonophysics*, *211*(1–4), 99–114. https://doi.org/10.1016/0040-1951(92)90053-9

Stover, C. W., & Coffman, J. L. (1993). *Seismicity of the United States, 1568-1989 (revised)* (Vol. 1527, p. 418). US Geological Survey Professional Paper. https://doi.org/10.1016/0148-9062(95)90013-6

Ulrich, F. P. (1941). The Imperial Valley earthquakes of 1940. *Bulletin of the Seismological Society of America*, *31*(1), 1–8. https://doi.org/10.1785/bssa0310010013

U.S. Geological Survey (USGS) and California Geological Survey. (2006). Quaternary fault and fold database for the United States. Retrieved from https://www.usgs.gov/natural-hazards/earthquake-hazards/faults

Vavra, E. J., Qiu, H., Chi, B., Share, P. E., Allam, A., Morzfeld, M., et al. (2023). Active dipping interface of the Southern San Andreas Fault revealed by space geodetic and seismic imaging. *Journal of Geophysical Research: Solid Earth*, *128*(11), e2023JB026811. https://doi.org/10.1029/2023JB026811

Vidale, J. E., & Shearer, P. M. (2006). A survey of 71 earthquake bursts across southern California: Exploring the role of pore fluid pressure fluctuations and aseismic slip as drivers. *Journal of Geophysical Research*, *111*(B5), B05312. https://doi.org/10.1029/2005JB004034

Waters, M. R. (1983). Late Holocene lacustrine chronology and archaeology of ancient Lake Cahuilla, California. *Quaternary Research*, *19*(3), 373–387. https://doi.org/10.1016/0033-5894(83)90042-X

Weldon, I. J., Fumal, T. E., Powers, T. J., Pezzopane, S. K., Scharer, K. M., & Hamilton, J. C. (2002). Structure and earthquake offsets on the San Andreas Fault at the Wrightwood, California paleoseismic site. *Bulletin of the Seismological Society of America*, *92*(7), 2689–2703. https://doi.org/10.1785/0120000612

Wessel, P., Luis, J. F., Uieda, L., Scharroo, R., Wobbe, F., Smith, W. H. F., & Tian, D. (2019). The generic mapping tools version 6. *Geochemistry, Geophysics, Geosystems*, *20*(11), 5556–5564. https://doi.org/10.1029/2019GC008515

Yang, W., & Hauksson, E. (2013). The tectonic crustal stress field and style of faulting along the Pacific North America plate boundary in southern California. *Geophysical Journal International*, *194*(1), 100–117. https://doi.org/10.1093/gji/ggt113

Yoshida, S., Koketsu, K., Shibazaki, B., Sagiya, T., Kato, T., & Yoshida, Y. (1996). Joint inversion of near- and far-field waveforms and geodetic data for the rupture process of the 1995 Kobe earthquake. *Journal of Physics of the Earth*, *44*(5), 437–454. https://doi.org/10.4294/jpe1952.44.437